

Cite this: *Chem. Soc. Rev.*, 2012, **41**, 1111–1129

www.rsc.org/csr

CRITICAL REVIEW

Layered nanocomposites inspired by the structure and mechanical properties of nacre

Jianfeng Wang,^a Qunfeng Cheng^{*a} and Zhiyong Tang^{*b}

Received 16th April 2011

DOI: 10.1039/c1cs15106a

Nacre (mother-of-pearl), made of inorganic and organic constituents (95 vol% aragonite calcium carbonate (CaCO_3) platelets and 5 vol% elastic biopolymers), possesses a unique combination of remarkable strength and toughness, which is compatible for conventional high performance materials. The excellent mechanical properties are related to its hierarchical structure and precisely designed organic–inorganic interface. The rational design of aragonite platelet strength, aspect ratio of aragonite platelets, and interface strength ensures that the strength of nacre is maximized under platelet pull-out failure mode. At the same time, the synergy of strain hardening mechanisms acting over multiple scales results in platelets sliding on one another, and thus maximizes the energy dissipation of viscoplastic biopolymers. The excellent integrated mechanical properties with hierarchical structure have inspired chemists and materials scientists to develop biomimetic strategies for artificial nacre materials. This *critical review* presents a broad overview of the state-of-the-art work on the preparation of layered organic–inorganic nanocomposites inspired by nacre, in particular, the advantages and disadvantages of various biomimetic strategies. Discussion is focused on the effect of the layered structure, interface, and component loading on strength and toughness of nacre-mimic layered nanocomposites (148 references).

^a Key Laboratory of Bio-inspired Smart Interfacial Science and Technology of Ministry of Education, School of Chemistry and Environment, BeiHang University, Beijing 100191, China. E-mail: cheng@buaa.edu.cn

^b Laboratory for Nanomaterials, National Center for Nanoscience and Technology, Beijing 100190, China. E-mail: zytang@nanoctr.cn; Fax: (+86) 10-6265-6765; Tel: (+86) 10-8254-5580

1. Introduction

Undergoing evolution for millions of years, many biological tissues and materials have realized perfect unification of their structure and mechanical properties. They are made of inorganic and organic constituents, arranged in complicated multiscale structures. Such structural materials possess a unique combination



Jianfeng Wang

inspired organic–inorganic composite materials with excellent mechanical properties.

Jianfeng Wang is currently a PhD student at Beihang University. He received his Bachelor's degree (2005) and Master's degree (2008) in Materials Science from Hunan University of China. In 2010, he joined Prof. Lei Jiang's group at Beihang University. His current scientific interests are focused on pursuing the impressive mechanical properties of biological materials, particular mother-of-pearl, understanding the relationship between their structure and properties, and fabricating bio-



Qunfeng Cheng

joined in BeiHang University. He is currently interested in lightweight, ultrastrong, and stiff nanocomposites based on carbon nanotubes and bio-inspired multi-functional, high performance organic–inorganic hybrid materials.

Qunfeng Cheng is currently an Associate Professor at School of Chemistry and Environment, BeiHang University. He received his PhD in Polymer Chemistry and Physics from Zhejiang University in 2008 under the supervision of Prof. Zhengping Fang and Prof. Xiaosu Yi. From 2008 to 2009, he worked with Prof. Shoushan Fan in Tsinghua University and Prof. Zhiyong Liang in Florida State University as a Postdoctoral Research Fellow. In 2010, he

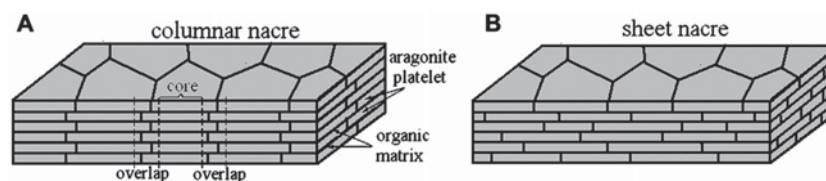


Fig. 1 Schematic illustration of the brick-and-mortar microstructure for (A) columnar nacre and (B) sheet nacre.

of light weight, good stiffness, remarkable strength and toughness, which is difficult to be achieved by artificial metallic, ceramic, polymeric materials and composites.^{1–4} One of the most outstanding examples is nacre, an inner layer of mollusc shells, which can be divided into two classes, Gastropoda and Bivalvia. It consists of 95 vol% fraction of aragonite calcium carbonate platelets, glued together with 5 vol% fraction of ductile biopolymer (proteins and polysaccharides).⁵ Although nacre mostly consists of a fragile mineral, its toughness is three orders of magnitude higher than that of calcium carbonate in the form of aragonite.⁶

1.1 Hierarchical structures of nacre

Nacre has hierarchical features that are found at different length scales. Its microscale architecture resembles a three dimensional brick-and-mortar structure,^{7–12} where the bricks refer to the densely stacked layers of aragonite with submicrometer thickness tightly held together by nanoscale biopolymer layers (Fig. 1). The brick-and-mortar structure shows two types of staggered arrangement, including columnar and sheet nacre (Fig. 1), which are observed from gastropods and bivalves, respectively. In the columnar nacre (Fig. 1A), platelets are stacked in columns with clear core and overlap regions, while the sheet nacre (Fig. 1B) exhibits a more random staggered arrangement without well-defined cores and overlap regions. The arrangement and size of platelets are highly uniform and compact (Fig. 2A). It should be noted that the platelets in both naces display an obvious waviness, rather than a flat plane (Fig. 2B).^{13–17} At mesoscale, the surfaces of tablets are rough with many nanoasperities of 10–30 nm in width and 100–200 nm in spacing, observed from both cross sections.¹⁸ Further detailed investigations at nanoscale reveal that mineral bridges between

the tablets are embedded in polymer layers (arrows in Fig. 2C),^{19,20} and meanwhile the nanograins on the tablets are delimited by the organic network (Fig. 2D).^{21,22} It is easily found that the hierarchical level of nacre is two-fold. The first level is that aragonite nanograins are glued together to form nanoplatelets. The nanoplatelets are staggered into a brick-and-mortar structure that is enveloped by biopolymer (the second level). Readers can refer to the excellent reviews to obtain more detailed information about the complex architectures of nacre.^{4,23}

1.2 Mechanical properties of nacre

The mechanical properties of nacre have been extensively studied from different aspects including tension,^{13,24,25} compression,^{18,26} shear,^{13,25} and bending.^{1,20} Moreover, the mechanical responses of its individual components have been tested by nanoindentation on single aragonite tablet^{17,18,27} and single-molecule force spectroscopy on single organic molecules.^{28,29} Among them, deformation under uniaxial tension along the direction of tablets is the most remarkable. The tensile strength and Young's modulus of nacre are in the range of 80–135 MPa and 60–70 GPa, respectively.^{1,18,20} The typical tensile behavior of nacre is shown in Fig. 3A, exhibiting a maximum strength of ~80 MPa and a relatively large plastic deformation.³⁰ At a tensile stress of about 70 MPa, the organic matrix starts to yield and the tablets locally slide on one another (Fig. 3). The nacre finally fractures in the form of tablet pull-out mode. To describe the mechanical response of biomaterials and structures, a variety of models have been proposed.^{13,31–33} Among them, an effective approach based on the mechanical properties of nacre has been successfully applied to quantitatively explain the relationship between the mechanical strength and brick-and-mortar structure.¹ The tensile strength has been described through a simple shear lag model. Owing to the robust interface between platelets, the interface strength (τ_i) is larger than the yield shear strength (τ_y). The ultimate tensile strength of the composite (σ_c) can be calculated as follows:

$$\sigma_c = V_p \sigma_p + (1 - V_p) \sigma_m \approx V_p \sigma_p \quad (1)$$

with V_p being the volume fraction of inorganic platelets and σ_p being the average tensile stress in a platelet.

A critical value (s_c) for the aspect ratio of platelets has been proposed:

$$s_c = \sigma_p / \tau_y \quad (2)$$

If the actual aspect ratio (s) is larger than the intrinsic critical value ($s > s_c$), fragile fracture dominates because breaking of platelets happens (Fig. 4A). Taking into account the interactions between neighboring platelets, σ_c follows that

$$\sigma_c = V_p \sigma_{pu} / 2 \quad (3)$$



Zhiyong Tang

Professor Zhiyong Tang obtained his PhD degree from Chinese Academy of Sciences in 2000 under the direction of Professor Erkang Wang. After finishing his postdoctoral training at both Swiss Federal Institute of Technology Zurich and University of Michigan, he came back to China and took a professor position at National Center for Nanoscience and Technology at the end of 2006. His main research interests are focused on preparation, assembly and application of functional nanomaterials.

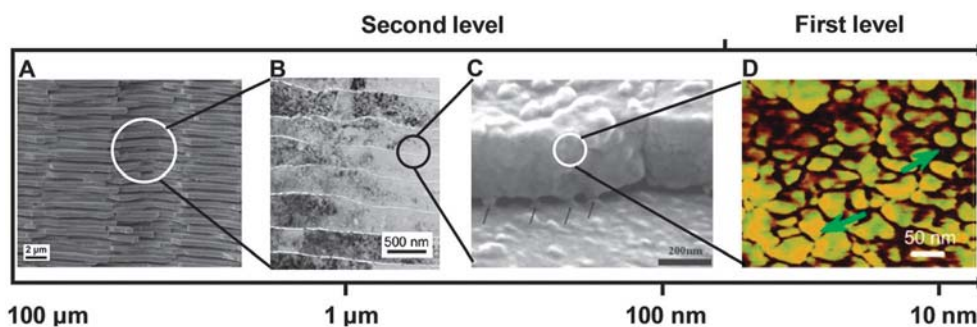


Fig. 2 Multiscale hierarchical organization in nacre showing at two structural levels: (A) cross section of abalone shell; (B) tablet waviness; (C) aragonite bridges (black arrows) and (D) nanograins separated by a nanoscale organic network. Adapted with permission from ref. 13 and 22.

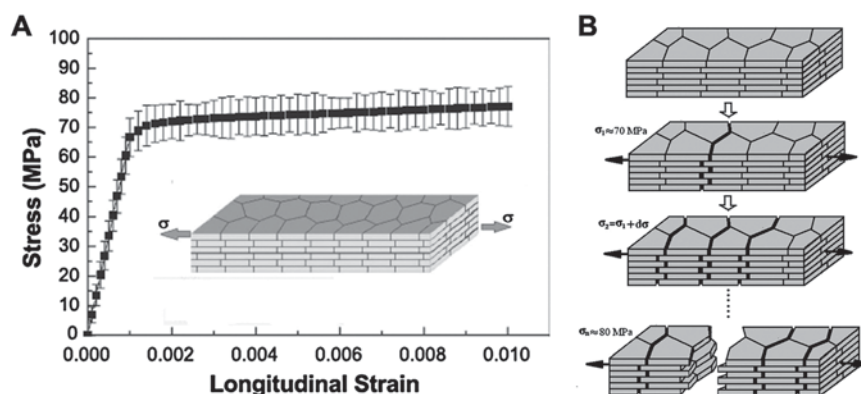


Fig. 3 (A) Typical stress-strain curve of nacre. (B) Schematic illustration of the plastic deformation process, due to strain hardening. Adapted with permission from ref. 30.

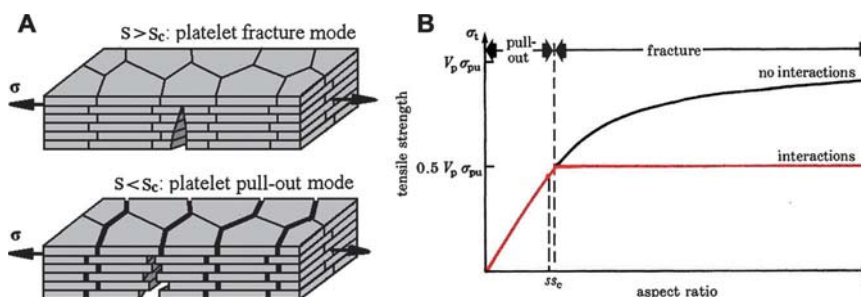


Fig. 4 (A) Fracture mechanisms and (B) theoretical variation of tensile strength of nacre with the aspect ratio of the platelets based on a shear lag model. Adapted with permission from ref. 1.

with σ_{pu} being ultimate breaking stress of platelets. For the platelets fracture without interactions, σ_c is given by

$$\sigma_c = V_p \sigma_{pu} (1 - s_c/2s) \quad (4)$$

Contrarily, when the aspect ratio is smaller than the critical value ($s < s_c$), the platelets start to slide on one another and are pulled out from the soft matrix (Fig. 4A). Having nothing to do with interaction between neighboring platelets, σ_c is follows:

$$\sigma_c = V_p \tau_y s/2 \quad (5)$$

The dependence of σ_c on s , s_c , V_p and σ_{pu} is summarized in Fig. 4B. It should be stressed that the interaction between platelets actually occurs because the aragonite bridges and nanoasperities act as reinforcements for the interface.^{20,33–36}

The theoretical analysis in Fig. 4B matches very well with the experimental measurements (Fig. 3A).

In general, composites with high volume fraction of inorganic components are strong but brittle and flaw-intolerant, due to platelet fracture prior to matrix yielding. Based on the design of fine brick-and-mortar structure and rational interface, the nacre was mineralized with aragonite calcium carbonate platelets of s slightly below s_c .¹ As a result, the natural composite fails under platelet pull-out mode and thus generates large fracture toughness, which will be discussed in detail below. At the same time, the ultimate strength can be maximized, because of extremely high mineral content, effective load transfer and optimum aspect ratio.

According to eqn (5), the theoretical strength of nacre calculated from structure parameters and the strength of the matrix is close to the experimental result.^{1,37} In terms of this

model, the strength of a single aragonite platelet is estimated to be more than 300 MPa. This is in keeping with the simulative strength of 350 MPa based on a discrete lattice model and an order of magnitude smaller than the theoretical value of a perfect aragonite crystal (~ 3 GPa).³⁸

Besides the strength, nacre also shows striking toughness. For example, the fracture of the hydrated shell of *Pinctada imbricate*, a bivalve mollusc, could reach 1.24 kJ m^{-2} , which is about 3000 times higher than that of monolithic CaCO_3 .¹ Meanwhile, the fracture toughness for red abalone is $8 \pm 3 \text{ MPa m}^{1/2}$ and is increased eightfold over pure monolithic CaCO_3 .³⁹ The detailed mechanism on the improved crucial toughness of nacre will be discussed in section 1.3 below.

1.3 Relationship of structure and mechanical property of nacre

Experimental results reveal that the mechanical properties of nacre, especially striking toughness, are highly dependent on their structures. The typical stress–strain curve presents a linear elastic region followed by a plastic deformation region before fracture (Fig. 3A). In the plastic deformation range, the strain accomplished by hardening reaches almost 1%, with thousands of microscopic tablets sliding on one another over a large volume. Notably, sliding of the platelets is not local but over a large volume through the specimen, which translates into relatively large strains at macroscale. So far, significant progress has been made to understand the crucial toughness of nacre. In earlier studies,^{1,24} a prevalent explanation was that the brick-and-mortar architecture led to highly tortuous crack paths with exposure of the local ceramic platelet surfaces. However, only brick-and-mortar architecture was insufficient to account for the high amount of energy dissipation that was experimentally measured. Subsequently, various mechanisms have been developed, including sliding of platelets and formation of organic ligaments between platelets,⁴⁰ the breakage of sacrificial bonds in the viscoelastic biopolymer at the molecular level,²⁹ crack deflection, branching and diversion,⁴¹ nanoasperities of the platelet interfaces^{20,31} and the breakage of aragonite bridges.^{4,35,42} As shown in Fig. 5A, a white process zone, an inelastic region ahead of the crack, was clearly observed using optical microscopy and reached approximately millimetre size in width.^{43,44} The stress whitening, a well documented phenomenon in nacre,^{20,24,25} originated from exposure of organic ligaments at the end of the separated tablets, which was an evidence of extensive tablets sliding. Furthermore, homogeneous tablets

separation was directly revealed by *in situ* atomic force microscopy (AFM) images (Fig. 5B and C).^{25,44} All these results indicate that the viscoplastic energy dissipation pervades through the full sample, rather than only at fracture surface.

Strain hardening, which is mainly ascribed to the obstacle preventing further sliding, is the key for large plastic deformation after linear elastic region. The working mechanisms at nanoscale (Fig. 6) and microscale (Fig. 7) for strain hardening include (i) aragonite asperities contact,^{20,33} (ii) mineral bridge relocking after fracture,^{4,23} (iii) the stiffening of biopolymer after elongation of $\sim 100 \text{ nm}$,²⁹ and (iv) the locking generated by the microscale waviness and dovetail of platelets.¹³ The surface waviness produced by the microstructure is an important feature that engenders hardening in nacre, which is confirmed by three-dimensional finite element models by Espinosa *et al.*¹³ The composite model containing wavy tablets exhibits large deformability that is close to experimental measurement on tension, whereas the model with flat tablets prematurely fails.

The organic materials at the interface withstand tremendous stretches, undergoing viscoplastically deformation and thus primarily dissipate energy.¹ Similarly to protein unfolding domains in bone,^{45,46} it is suggested that proteins in nacre, acting as high performance adhesive, also include folded modules that can be unfolded sequentially under load.²⁹ The load-extension of a single protein exhibits a sawtooth-like pattern, where each peak corresponds to the sequential unfolding of the modules. Schaffer *et al.*⁴⁷ and Song *et al.*^{35,42} proposed that the combination of mineral bridges with such biopolymer adhesive was the main mechanism leading to the striking toughness. Li *et al.*²² found that the spacing between nanograins in the first hierarchical level increased under tension and that the viscoelastic-plastic biopolymer between nanograins was stretched. It was accompanied by nanograin rotation and deformation that contributed to energy dissipation.

The experimental observation of the structural change of abalone shell under strain has addressed several important features related to its toughness. The elongation of folded protein is about 100 nm before stiffening. The nanoasperities and aragonite bridges are 100–200 nm in spacing. The inelastic deformation of nacre in tension is about 1%, which agrees with tablet (about 9 μm in diameter) sliding (100 nm) in a homogenous fashion.^{25,44} The above results indicate that all four mechanisms most likely act in a synergetic way. In the first step, strain hardening emerges locally after a tablet somewhere starts to slide about 100 nm at a tensile stress of

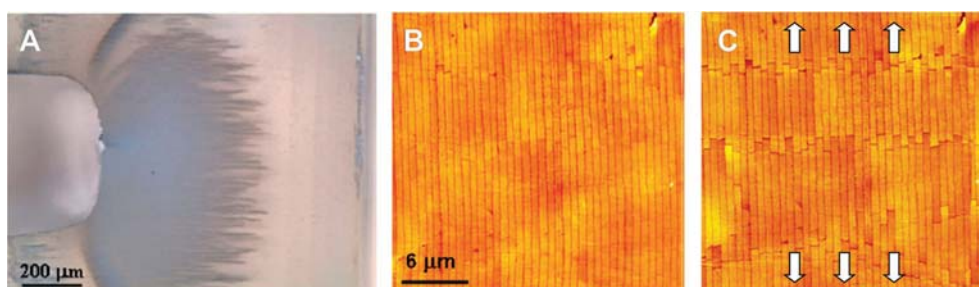


Fig. 5 (A) Optical image of columnar nacre from a four point bending test, showing a relatively homogeneous inelastic region. *In situ* AFM imaging ahead of a propagating crack of top shell (B) before and (C) after deformation, showing that all the junctions are open, due to uniform tablet sliding. Adapted with permission from ref. 44.

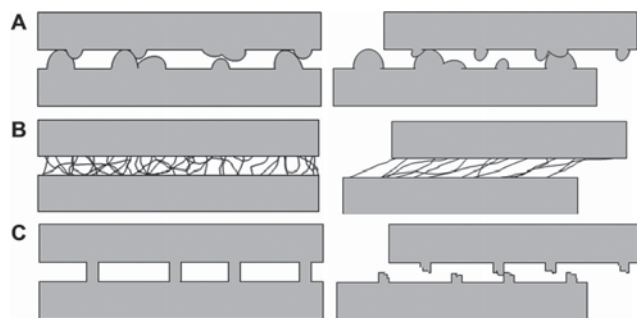


Fig. 6 Three types of nanoscale models controlling the frictional resistance to the sliding of platelets. (A) Nanoasperities contact after platelets sliding over a certain distance. (B) Biopolymer stiffening after the breaking of sacrificial bonds. (C) Fractured mineral bridges contact over again, akin to the mechanism of nanoasperities. Adapted with permission from ref. 36.

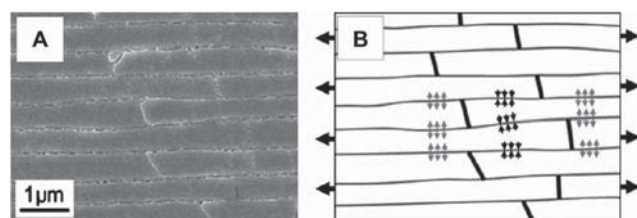


Fig. 7 Microscale mechanism controlling the frictional resistance to sliding of platelets. (A) Scanning electron microscopy (SEM) image of the cross section of nacre, showing a few dovetail like features and waviness of platelets. (B) Outline of the tablet contours, showing normal compression (black arrows) at overlap regions and equilibrium of forces at core regions under tensile loading. The normal compression generates additional resistance to tablet sliding. Adapted with permission from ref. 25.

about 70 MPa (Fig. 3B). The enhanced stress is transferred to a vicinal one along the tablet, which subsequently slides over the same distance and then generates another local strain hardening. Such sliding and strain hardening are accumulative in a step fashion and spread parallel to the tablets until the material fails under platelet pull-out mode. Besides viscoplastic deformation of the large scale adhesive layers between microscopic platelets in the second hierarchical level, the plastic deformation of the fine organic network in the first hierarchical level may also occur in a large volume, due to the strain hardening. Therefore, the large amount of energy dissipation might be attributed to the viscoplastic deformation of both inter-platelet and intra-platelet biopolymers in a synergy of multiple scales. Together with shear lag model and toughness analysis of nacre, some basic principles for design of biomimetic material can be outlined. (i) Hierarchical structure is the prerequisite. (ii) The strength of inorganic platelet must be as high as possible. (iii) The volume fraction of the platelets is high enough. (iv) High interface adhesion and shear strength must be needed. (v) The aspect ratio is as high as possible before the critical value is reached. (vi) The strain hardening at micro- and/or nanoscale should occur in order to spread plastic deformation of the matrix throughout the material.

Inspired by the perfect integrated feature of the hierarchical structure and mechanical properties of natural nacre, scientists

put forward the questions whether artificial materials with similar structures and equal or even better properties can be produced. Humans have the ability to create and make use of more elements and stronger building blocks for copying the complex structure of nacre, while the components of biomaterials are restricted by the ambient environment (water, mineral, iron, and so on).³ On the other hand, many processing methods and extreme synthetic conditions, which biological tissue and materials do not undergo, may be utilized, for example extreme pH, temperature and pressure. As a consequence, the artificial materials can be likely to achieve unprecedented mechanical properties by assembling strong building blocks and mimicking nacre's structure.

2. Synthesis strategies to bioinspired composites

Creation of artificial nacre materials with strong mechanical properties needs design of the hierarchical structure, control over the content of inorganic phase, optimization of interface, and development of assembly procedures. In the following section, we summarize recent progress in the field of mimicking the architecture of nacre. The fabrication methods are divided into six categories: (1) conventional method for bulk ceramic materials, (2) freezing casting, (3) layer-by-layer deposition, (4) electrophoretic deposition, (5) mechanical assembly and (6) chemical self-assembly. The conventional method for bulk ceramic materials is good for assembly of several hundreds of micrometre thick platelets, more than two orders of magnitude thicker than aragonite platelets ($\sim 0.5 \mu\text{m}$). Assembly of inorganic layers of several micrometre thickness is best realized through a freezing casting technique. Layer-by-layer deposition and electrophoretic deposition are limited to prepare ultrathin films with nanometre-thick tablets. Both bulk materials and thin films can be fabricated rapidly using mechanical assembly, and the sizes of platelet building blocks vary from the nanometre to micrometre range. Instead of pre-existing inorganic building blocks, chemical self-assembly is suitable for fabricating nacre's analogs from molecular precursors, more close to the natural processing of biological materials. Synthetic materials reported in the literature with robust interfaces, ordered layered microstructures and excellent mechanical properties are highlighted.

2.1 Conventional method for bulk ceramic materials

A major obstacle that limits the application of ceramics is their brittleness, owing to the sensitivity to the existing flaws. Usually, there are two approaches to increase the toughness. One is to eliminate the flaws produced by organic inclusions, dust or agglomerated particles, or at least to reduce their sizes, because they are difficult to be entirely removed. The other method is to prepare composites *via* addition of fibers, whiskers or particles reinforcements, and zirconia phase transformation reinforcing, *etc.* Unfortunately, the improvement of mechanic properties is limited by using both methods. Inspired by the nacre structures, an alternative way to synthesize the toughening ceramics is suggested by using layered structures instead of disordered compositions. Sarikaya and Aksay⁴⁸ made the first attempt to mimic the structures of nacre in 1990s, and the prepared Al-B₄C laminate was five times tougher than monolithic B₄C. In 1990, Clegg *et al.*⁴⁹ developed

a simple way to produce continuous layered silicon carbon material that contained weak graphite interface. Silicon carbide powders doped with boron were made into sheets of $\sim 200\ \mu\text{m}$ thickness. The sheets were coated with graphite and then pressed together, followed by sintering without pressure. The fracture toughness reached $15\ \text{MPa m}^{1/2}$, which was a fourfold increase in toughness relative to monolithic silicon carbide. The work of fracture increased more than a hundredfold, reaching $4625\ \text{J m}^{-2}$, which is a breakthrough in development of tough ceramic matrix composites. In principle, it reduces the dependence of the toughness of silicon carbide material on pre-existing cracks through the energy dissipation mechanism, thereby imparting flaw tolerance to the classically brittle ceramic.

Hereafter, various methods including tape casting and slip casting have been applied to prepare continuous multilayered ceramic materials with relatively weak interlayers. The developed weak interlayers mainly include plastic resin,^{15,50,51} graphite,⁵² boron nitride,^{53–59} and porous ceramic layers.^{60,61} Many studies have been conducted in different types of materials, e.g. alumina/zirconia,^{62–67} alumina/aluminum titanate,⁶⁸ mullite/alumina,⁶⁹ silicon carbide,⁷⁰ silicon nitride,⁷¹ and silicon carbide/carbon.⁷² Such composites obviously possess improved fracture toughness, and meanwhile maintain a high level of strength. It is found that appropriate design of the interphase, which prevents crack deflection, is the most important factor in fabricating materials with such properties. Li and Wang *et al.*⁵⁹ investigated the effect of the strength of interfacial layers on fracture behavior of laminated $\text{Si}_3\text{N}_4/\text{BN}$ composites. The interface strength was tailored by addition of Si_3N_4 between BN layers. Compared with the interfacial layers with 5% Si_3N_4 (Fig. 8A), stronger BN interfacial layers containing 50% or 10% Si_3N_4 made the crack deflection more difficult (Fig. 8B and C). *In situ* observation of cracking of the laminar composite containing 5% Si_3N_4 within the weak interface layer was conducted by integrating a custom-designed micro-mechanical tester with an optical microscope and an atomic force microscope. The original microvoids and microcracks arrested the major crack, resulting in crack deflection and extension within the relatively weak interfacial layers. The fracture process was explored to undergo four stages (Fig. 8D). After linear elastic deformation, a crack initiated, and then deflected and propagated in a stable fashion within the BN interfacial layers, forming a T-shaped crack path. Subsequently, the crack unstably propagated in both matrix and interfacial layers with crack deflection, kinked out of the interfacial layers, and penetrated Si_3N_4 layers time after time until fracture. Based on *in situ* observation of crack extension, the scheme of its three-point bending load–displacement curve is shown in Fig. 8E.

Mayer further utilized the high-performance engineering materials to build large scale analogs.⁷³ Alumina plates (0.04 inch in thickness) were bonded with strong silicone adhesives or tape adhesives of the acrylic family. It was found that too strong (silicone adhesive) and too thick adhesives were detrimental to the toughness, due to lack of significant crack divergence. On the contrary, a low volume fraction of the VHB™ Adhesive Transfer Tape 9473-PC exhibited remarkable resilience with extensive ligament formation.

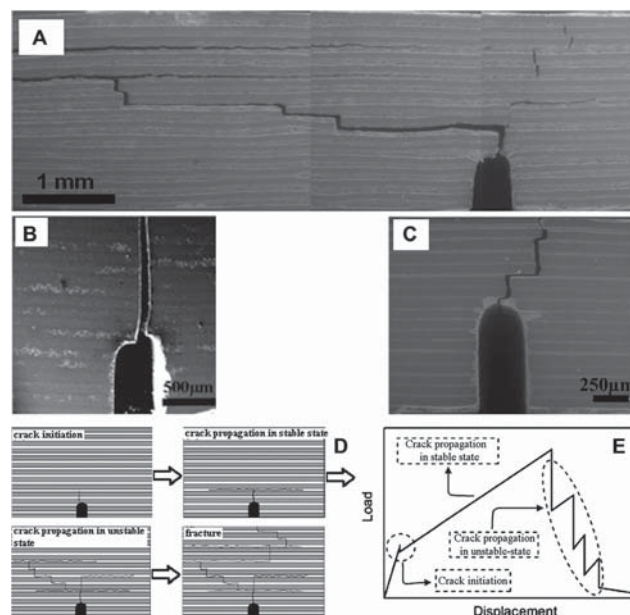


Fig. 8 SEM images of three fractured $\text{Si}_3\text{N}_4/\text{BN}$ composites with BN interfacial layers. (A) Containing 5% Si_3N_4 , showing a stable crack deflection. (B) Containing 50% Si_3N_4 , showing a straight crack without any crack deflection. (C) Containing 10% Si_3N_4 , showing an unstable and limited crack deflection. (D) Scheme of crack extension in laminar $\text{Si}_3\text{N}_4/\text{BN}$ composites with BN interfacial layers containing 5% Si_3N_4 . (E) The scheme of its three-point bending load–displacement curve, based on *in situ* observation of crack extension. Adapted with permission from ref. 59.

Although the composite with continuous layers had a higher strength, a segmented layer with 89 vol% ceramic was six times tougher than monolithic alumina beam, and showed a nearly two-fold increase in toughness of the continuous-layered beam. The crack propagation path of the brittle segmented composites with 82 vol% alumina was not reported. The result suggested that there was an optimum content of the organic phase, and exceeding or lowering this value resulted in reduction of the energy dissipation.³

Recently, on the basis of quantitative analysis of aragonite tablet sliding and waviness-induced interfacial hardening mechanisms of natural nacre, Espinosa *et al.*⁷⁴ designed scale-up ABS/epoxy model composites with dovetailed ABS platelets (thickness, $t = 1.85\ \text{mm}$), as shown in Fig. 9A and B. ABS platelet geometries were optimized by varying dovetail angle and dovetail overlap length (Fig. 9C and D). The absence of interfacial hardening mechanism led to little hardening and low strength (sample 1). Too short dovetail length generated softening and platelet pull-out failure mode, exhibiting low energy dissipation (sample 3). Excessively great interfacial hardening strength promoted localized platelet brittle fracture (sample 4). Sample 2 with appropriate dovetail angle and length ($\theta = 1^\circ$, $L/t = 3.1$) possessed clear dilation-induced strain hardening, that was, the greatest degree of sliding, highest strength and toughness. Notably, the ABS platelet geometry in sample 2 fell within the range of platelet geometry in nacre (Fig. 9E), indicating that the optimized model composite had a similar mechanism to that of Nature's evolution process. Akin to natural nacre, platelet sliding in the overlap region for the

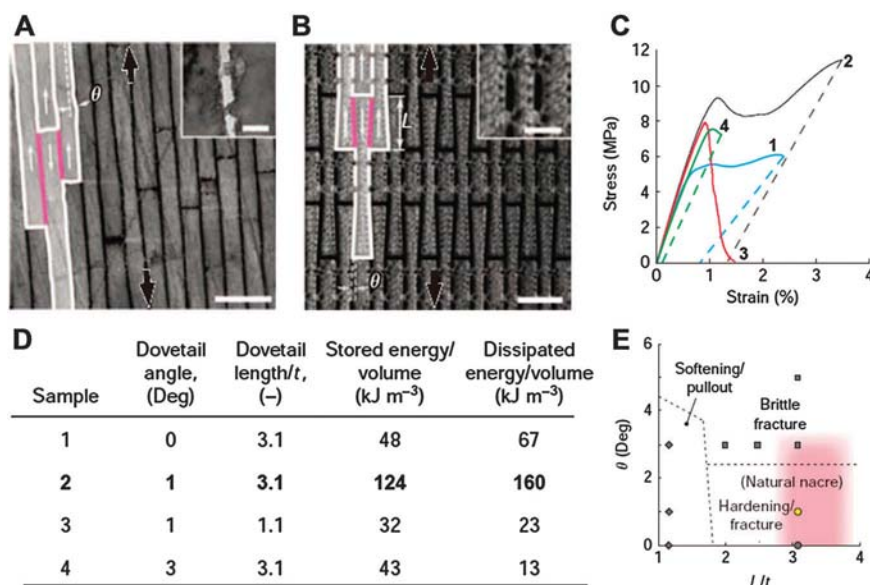


Fig. 9 (A) SEM image of columnar nacre (red abalone shell) showing microstructure and platelet sliding at overlap regions under loading. Scale bar: 1 μm . Inset shows the transmission electron microscopy (TEM) image of aragonite bridges. Scale bar: 100 nm. (B) Nacre-inspired ABS/epoxy composites showing dovetailed ABS platelets; L and θ represent the dovetail length and angle, respectively. Scale bar: 5 mm. Inset shows the detail of the inter-platelet bridges. Scale bar: 2 mm. (C) Tensile stress–strain curves for ABS/epoxy samples with different L and θ (labeled by sample number as listed in D). Sample 2 exhibits best strength and toughness among these designed composites. (D) Table showing stored and dissipated energies for samples of varying tablet geometries (length = 5.7 mm, width = 2.1 mm, thickness = 1.85 mm). (E) Parametric map of failure modes for ABS/epoxy composites as a function of tablet geometry. Sample 2 is indicated with a yellow-filled circle that falls within the range of aragonite platelet geometries of nacre. Adapted with permission from ref. 74.

optimized artificial nacre spread over large areas, increased with progressive loading, and then partially relaxed on failure.

In brief summary, the improvement of fracture toughness is successfully achieved for synthetic laminated ceramic materials, but the results are not as prominent as for natural nacre. One of the reasons may be the design of these laminates is still at the micrometre scale level ($>100 \mu\text{m}$), which far surpasses the thickness of monolithic CaCO_3 layers in nacre (about $0.5 \mu\text{m}$). Thinner layers can increase tortuous crack propagation distance and promote more energy dissipation.

2.2 Freezing casting

Fortunately, laminar composites with several micrometre-thin ceramic layers can be fabricated by the freezing casting method. This technique was developed by Deville *et al.*⁷⁵ to build homogeneous, layered and porous scaffolds by taking advantage of the physics of ice formation. There exists a critical particle size during freezing of dilute suspensions. Above the critical value, the suspended particles are trapped by the moving water–ice front. Furthermore, the hexagonal ice crystals have strong anisotropic growth kinetics. Based on these two characteristics, the authors designed an experimental setup to precisely control the freezing kinetics. Directional freezing of the alumina slurries was achieved by a temperature gradient in the direction parallel to the movement of the freezing front. Interestingly, particles trapped in between the ice dendrites gave rise to surface roughness and ceramic bridges between layers, akin to the asperities and mineral bridges of nacre. Subliming the ice by freeze drying produced a ceramic scaffold and its microstructure was a negative replica

of the ice. Furthermore, the thickness of layers could be controlled from 1 μm (close to that of aragonite platelets in nacre, approximately $0.5 \mu\text{m}$) to 200 μm by changing the freezing kinetics. After the porous scaffolds were filled with a second phase, Al–Si, a dense bulk material was fabricated and exhibited extensive crack deflection at the interface, resulting in increased toughness. The mechanical response of alumina–Al–Si (45/55 vol%) layered composites increased from 400 to 600 MPa for strength and from 5.5 to 10 $\text{MPa m}^{1/2}$ for fracture toughness, when the chemistry of interface was tailored by adding a small amount of Ti to the aluminum alloy. The toughness was more than twice higher than alumina (3–5 $\text{MPa m}^{1/2}$). Compared with natural nacre, the obtained volume fraction of ceramic phase is still low.

Munch *et al.*⁷⁶ added sucrose to the alumina slurry to modify the viscosity and phase diagram of the solvent, resulting in the formation of ice crystals with a characteristic microscopic roughness (Fig. 10A and B) and bridge density. The porous scaffolds were filled with a sacrificial second phase, followed by pressing the scaffolds in the direction perpendicular to the lamellae and then sintering them. As a result, the continuous layer structures were transformed into brick-and-mortar scaffolds (Fig. 10B). The pressing and sintering promoted densification and formation of ceramic bridges between the bricks. The brick-and-mortar scaffolds were chemically modified with 3-(trimethoxysilyl)propyl methacrylate and then infiltrated with polymethyl methacrylate (Fig. 10C). The thickness of the organic layer ranged between 10–20 μm in lamellar structures prepared by directly infiltration with polymethyl methacrylate, while it was only 1 μm in the brick-and-mortar materials. Surprisingly, the volume fraction

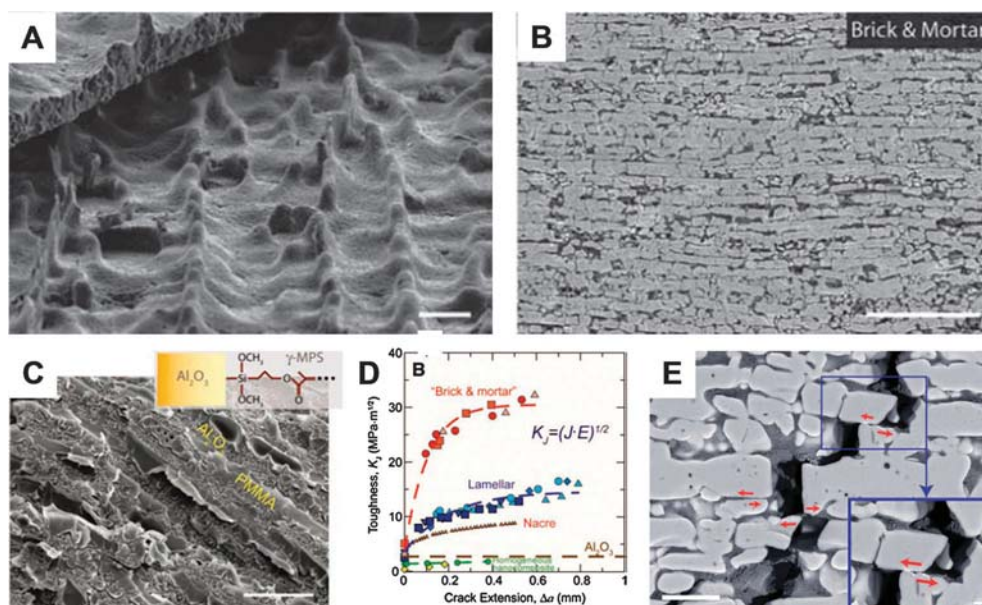


Fig. 10 Structure, interface and toughening mechanisms of ice-templated materials. (A) Brick-and-mortar architecture. (B) Microscopic roughness in the ceramic walls. (C) Chemical grafting leads to flat fracture surfaces. (D) Rising R-curve behavior, akin to nacre. (E) Pull-out failure mode of ceramic bricks. Arrows indicate the direction of frictional sliding between ceramic bricks. Scale bars: 10 μm (A), 100 μm (B), 5 μm (C), 10 μm (E) and 2 μm (the inset in E) Adapted with permission from ref. 76.

of ceramic phase was as high as 80% in the brick-and-mortar materials. On account of the hierarchical design, optimized interface and considering high content of alumina, the material showed a unique combinations of high strength and large fracture resistance. The flexural strength reached 210 MPa, which was comparable to that of alumina prepared by slip casting. The elastic modulus was calculated to be 115 GPa, in the direction perpendicular to the ceramic layers.⁷⁷ In addition, the plane strain fracture toughness was almost twice as high as that of a simple mixture of Al_2O_3 and PMMA. More importantly, the multiscale toughening led to rising R-curve behavior, similar to nacre (Fig. 10D). Although containing $\sim 80\%$ alumina, the material exhibited a high degree of inelasticity and ultimate strain reached 1.4%. Notably, the strength, modulus and toughness of the ice-templated materials all exceeded those of nacre. The fracture path of the hybrid material clearly demonstrated the extensive crack deflection, resulting in a “platelet pull-out” failure mode (Fig. 10E).

Recently, continuous layered scaffolds prepared by freezing casting were infiltrated with a metal with a low melting point and viscosity, Al–Si eutectic alloy.⁷⁸ The low contact angle of the alloy on alumina, approximately 50° in vacuum, facilitated infiltration at relatively low pressures and inorganic bridges and surface roughness were generated. The $\text{Al}_2\text{O}_3/\text{Al-Si}$ hybrid composites containing alumina and Al–Si lamellae with different thickness, *e.g.* 10/20 and 25/50 (numbers corresponding to the Al_2O_3 and Al–Si lamellae in μm , respectively), were investigated. Relatively flat fracture surfaces were observed, implying strong bonding between Al_2O_3 and Al–Si. Both hybrid materials exhibited slightly higher strength than that of pure Al_2O_3 and Al–Si. The 10/20 and 25/50 composites had a similar fracture toughness for crack initiation and displayed R-curve behavior, but the fracture toughness of the coarse structure reached approximately $40 \text{ MPa m}^{1/2}$,

which was almost twice higher than that of refined structure (about $22 \text{ MPa m}^{1/2}$). Interestingly, the fine 10/20 composite showed single crack-propagation mode (Fig. 11A), while multiple crack-propagation mode was observed for the coarse 25/50 composite (Fig. 11B). It is noted that multiple fracture is somewhat akin to the result of the strain hardening in nacre (Fig. 11C and D). The “multiple cracking” fracture mode with greater distribution of damage leads to significantly higher

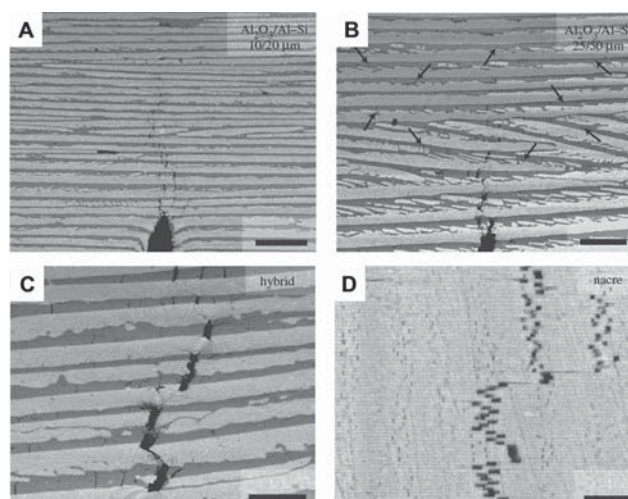


Fig. 11 Fracture mode transition. (A) Multiple cracking fracture mode in $\text{Al}_2\text{O}_3/\text{Al-Si}$ (10/20 μm) continuous laminar composite. The arrows indicate the presence of the microcracks. (B) Dominant single cracking fracture mode in $\text{Al}_2\text{O}_3/\text{Al-Si}$ (25/50 μm) continuous laminar composite. (C, D) Comparison of the mechanism of damage in $\text{Al}_2\text{O}_3/\text{Al-Si}$ (25/50 μm) hybrid composite and hydrated red abalone shell. Damage spreading in (C) synthetic material is similar to that observed in (D) nacre. Scale bars: 200 μm (A) and (B), 100 μm (C) and 5 μm (D). Adapted with permission from ref. 78.

toughness than single fracture, indicating that crack deflection is insufficient to guarantee nacre-like behavior. It is elucidated that an increase of metal layer thickness reduces the stress in the intact layer ahead of the crack tips, leading to a transition from single to multiple cracking. So the deformation mechanisms of $\text{Al}_2\text{O}_3/\text{Al-Si}$ hybrid composites are different from nacre.

2.3 Layer-by-layer deposition

Layer-by-layer (LBL) assembly is a versatile and elegant technique for fabricating structured and functional thin films by alternately immersing a clean substrate into two solutions, which can interact and assembly accumulatively upon varying the driving force. The driving forces mainly include electrostatic interaction, hydrogen bonding, charge transfer, covalent bonding, and hydrophobic interaction. LBL can be used to combine hard inorganic species with soft organic phase, thus merging the properties of each type of materials. It allows accurate control over materials' structure and is capable of incorporating high loading of inorganic fillers in hybrid materials. Hence, the layered structure of nacre is easily copied by LBL techniques.

Layered silicates are used extensively to prepare segmented layered nanostructures because of low cost and the high strength of individual nanosheets. The in-plane modulus of elasticity of montmorillonite (MTM), one of typical layered silicates, is determined and reaches ~ 270 GPa by molecular dynamics simulation.⁷⁹ The general formula for the class of MTM is $(\text{Na,Ca})_{0.33}-(\text{Al}_{2-y},\text{Mg}_y)\text{Si}_4\text{O}_{10}(\text{OH})_2 \cdot n\text{H}_2\text{O}$. One individual MTM nanosheet of the layered solid consists of two layers of corner-shaped tetrahedra of Si^{4+} and one layer of the intervening octahedra of Al^{3+} or Mg^{2+} , the thickness of which is approximate 1 nm and both length and width are

more than 100 nm. Due to their capacity for substitution of various atoms in tetrahedral and octahedral layers, such as Al^{3+} by Mg^{2+} and Si^{4+} by Al^{3+} , a net negative charge of the sheets is generated, which allows LBL assembly with oppositely charged polyelectrolytes upon the electrostatic attraction.

Although considerable increase in stiffness and strength with low content of MTM nanoplatelets has been achieved by conventional blends,⁸⁰ the expected theoretical maxima at high platelet concentration cannot be achieved experimentally.^{81,82} Further increase of platelet concentration even brings about a sharp decrease in strength and brittle fracture for polymer composites. The decrease is mainly ascribed to the difficulty of exfoliation into single nanosheets at large volume fraction of inorganic tablets, a weak organic-inorganic interface and lack of the controllable arrangement of nanoplatelets. LBL assembly allows us accurate control over structure of the composite and incorporation of high loading of fillers into hybrid materials, and thus can be used to resolve the long-standing problem in MTM/polymer composites. Kleinfeld *et al.*⁸³ and Kotov *et al.*⁸⁴ reproduced layered seashell structures by LBL assembly of cationic poly(diallyldimethylammonium chloride) (PDPA) and anionic MTM nanoplatelets. In order to duplicate the ordered brick-and-mortar arrangement and the ionic cross-linking of tightly folded biopolymer of nacre, Tang *et al.*⁸⁵ prepared MTM/PDPA nanocomposite by sequential deposition. Owing to the strong attractive electrostatic and van der Waals interaction at the interface, the MTM platelets with a thickness of 0.9 nm were compatible with macromolecules and arranged parallel to the surface of film to maximize the attractive energy. A segmented layered microstructure with layer waviness was obtained, as seen in Fig. 12A. AFM imaging further revealed that the PDPA chains, which were adsorbed on the MTM

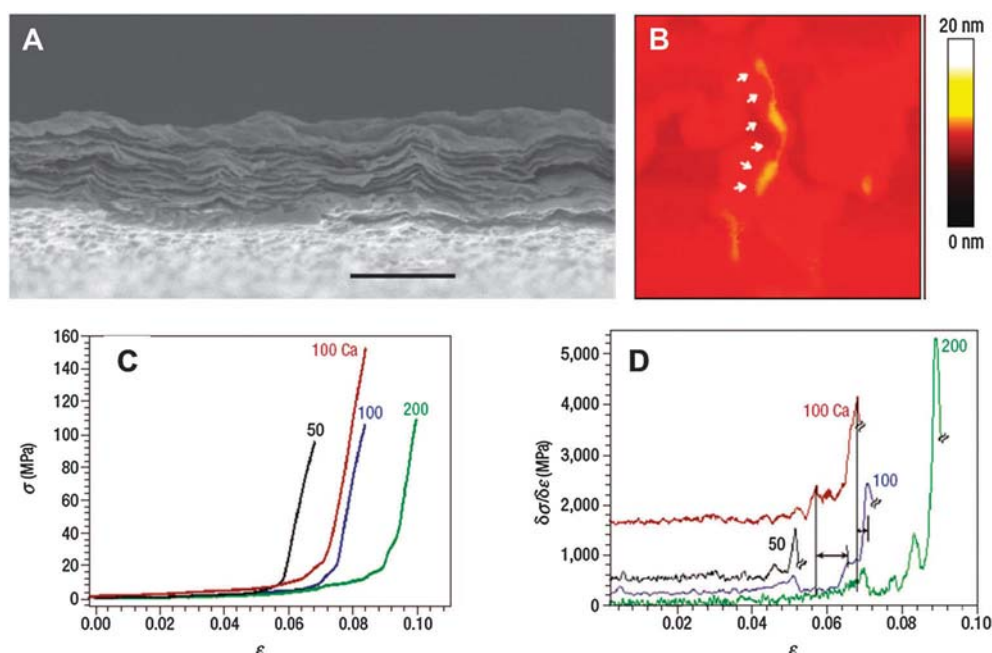


Fig. 12 Microstructure and mechanical properties of MTM/PDPA composite film. (A) SEM image of an edge of the film. Scale bar: 2 μm. (B) AFM image of PDPA molecules adsorbed on the MTM platelets. (C) Stress–strain curves of free-standing films made from (P/C)₅₀, (P/C)₁₀₀, (P/C)₂₀₀ and (P/C)₁₀₀ ion-exchanged with 1 M $\text{Ca}(\text{NO}_3)_2$ for 24 h. (D) The derivatives of the stretching curves in the low- and intermediate-stress regions, revealing the sawtooth pattern. Adapted with permission from ref. 85.

nanoplatelets, existed in a tightly coiled conformation (Fig. 12B). After a large plastic deformation under low stress, abrupt hardening was observed (Fig. 12C). The differential form of the stretching curves presented sawtooth-like behavior (Fig. 12D), which was also observed with the stretching of biopolymer in nacre by single-molecular force spectroscopy.²⁹ While the initial linear elastic region was attributed to the disruption of weak short-range van der Waals interaction, the hardening region was assigned to the sequential breakage of the stronger ionic bonds of different characteristic energy when the platelets sided on one another. The tensile strength and stiffness reached 106 MPa and 11 GPa, respectively, which was very closed to that of natural nacre.

To enhance the interface strength and improve the load transfer from matrix to MTM platelets, Podsiadlo *et al.*^{86–89} did a series of experiments for tailoring the platelet–polymer interface chemistry, and selection of polymer matrixes and cross-linking agents. Initially, a higher strength was expected by replacing relatively weak PDDA ($\sigma = \sim 12$ MPa) with a much stronger biopolymer, chitosan ($\sigma = \sim 108$ MPa).⁸⁶ A uniform film with a rather high loading of MTM (~ 80 wt%) was successfully prepared. However, the ultimate strength was only 80 MPa, which was lower than those of chitosan and the assembly film of PDDA/MTM. This was attributed to the molecular rigidity of the chitosan backbone, leading to adsorption on MTM surfaces in highly elongated configuration of molecular chain, which was obviously different from the coiled configuration of PDDA in composites (Fig. 13). Due to the molecular rigidity, plane-to-plane adhesion revealed a factor of ~ 4 lower strength as compared with PDDA/MTM nanocomposite. Alternatively, DOPA (L-3,4-dihydroxy-phenylalanine) molecules, imparting high adhesive strength to the MTM surface, was used to enhance the strength of DOPA-based MTM nanocomposite with 65 wt% nanoplatelets.⁸⁷ The strong self-crosslinking in the presence of Fe^{3+} led to twice higher strength than PDDA/MTM layered nanocomposite. Compared with nacre, the strength and toughness of DOPA/MTM was increased two and three times, respectively. However, its modulus was only 40% of that of natural nacre.

Another selected polymer was poly(vinyl alcohol) (PVA), and the staggered layered structure like nacre is shown in Fig. 14A. PVA forms highly efficient hydrogen bonding and cyclic cross-linking to Al substitution both on the MTM sheet surface and at the edge of the MTM sheet (Fig. 14B).⁸⁸

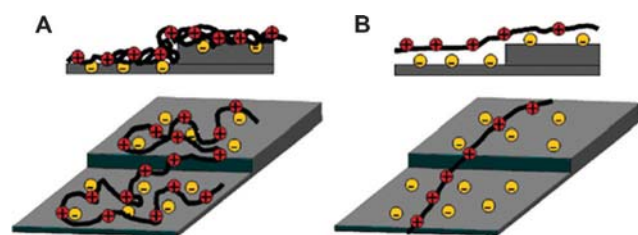


Fig. 13 Scheme of adsorbing polyelectrolyte chains with the folded and presumed structures. (A) PDDA/MTM. (B) Chitosan/MTM nanocomposites. Top images represent a side view of an edge of a MTM nanosheet adsorbed on a substrate. Adapted with permission from ref. 86.

The tensile strength and modulus reached 150 MPa and 13 GPa, respectively, for the composites with 50 vol% of MTM. Impressively, the treatment with glutaraldehyde, a cross-linking agent for PVA, gave rise to a drastic increase in strength and modulus, reaching 400 MPa and 106 GPa, respectively. At the same time, the material had a brittle fracture with only 0.33% ultimate strain. Recently, another cross-linking approach for PVA, ionic cross-linking by Cu^{2+} or Al^{3+} , was used to treat the LBL film of nacre-like nanocomposite with ~ 50 vol% MTM.⁸⁹ A double network of sacrificial bonds, *i.e.* hydrogen and van der Waals bonds between MTM and PVA and intramolecular ionic bonds introduced by metal cations, were proposed. The hydrogen and van der Waals bonds were broken and reformed when MTM nanotablets slid against each other, similarly to ionic bonds in nacre and PDDA/MTM nanocomposites. Once again, the characteristic sawtooth pattern in the differential strain curve, typical for biopolymers in nacre, was observed for the non-crosslinked film. After cross-linking, the tensile strength increased from 150 to 320 MPa, which was more than twice as high as that of nacre. The modulus increased from 13 to 60 GPa, which approached to that of nacre. The same disadvantage was that the strain ($\sim 0.3\%$) was lower than that of nacre (1%). These results highlight the tremendous promise of nacre-mimetic high-strength nanocomposites with high loading of ceramic phase obtained by the LBL assembly method.

However, the practical application of these materials prepared by the conventional LBL technique is limited because of time-consuming sequential deposition. To overcome the slow deposition speed, MTM nanosheets were successfully incorporated into exponential LBL assembly of poly(ethyleneimine) and poly(acrylic acid).⁹¹ The film growth rate was about 100 times faster than linear LBL. The prepared nacre-like analogue had high hardness and modulus, which reached 0.88 and 16 GPa, respectively. The content of MTM was dramatically lower compared with the products from linear LBL and was only as high as ~ 10 wt%. PDDA/laponite layered composites with about 60 wt% of inorganic material were recently prepared using spin-assisted LBL by Vertlib *et al.*⁹² The hardness and modulus values of the film with the controlled layered structure were maintained, and the speed was 10 times compared with traditional dip-coating LBL process.

Studart *et al.*³⁷ fabricated alumina/chitosan films by sequential deposition of inorganic and organic layers. Amine-modified submicrometer alumina platelets were first assembled at the air–water interface into an oriented two-dimensional monolayer by colloidal-based techniques. Afterwards, the two-dimensional monolayer was transferred to a substrate by dip-coating followed by spin coating with an organic layer of chitosan solution. The resulting hybrid films exhibited brick-and-mortar structures with strongly aligned and evenly dispersed platelets. In the light of the design principle of nacre discussed in the previous section, the ultrastrong alumina platelets of the aspect ratio slightly below the critical value were used to maximize the strength under platelet pull-out failure mode (Fig. 15A). Five times higher aspect ratio of alumina platelets (~ 40) than aragonite platelets in nacre (~ 8) and comparable matrix strength made the synthetic composite with 15 vol% platelets stronger than

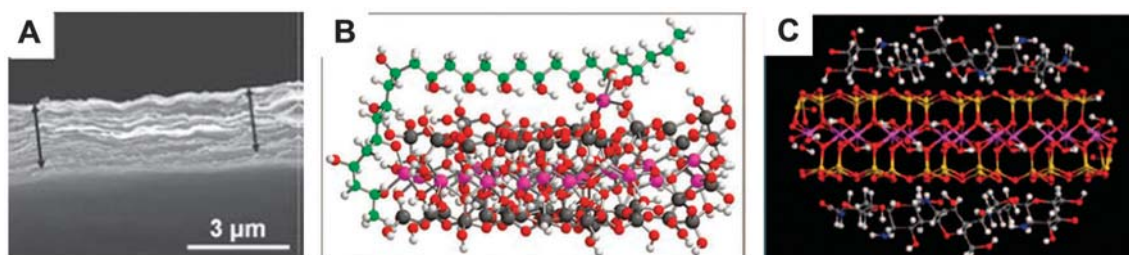


Fig. 14 (A) SEM images of a free-standing PVA/MTM layered nanocomposite. (B) Energy-optimized geometry of bonding between PVA and MTM via Al substitution sites (obtained by computer calculation of the AM1 semi-empirical algorithm): Al, purple; O, red; H, light gray; Si, dark gray; C, green. (C) Atomic modeling of interaction between MTM and chitosan molecules. Al, purple; Si, yellow; O, red; C, gray; N, blue; H, white. Adapted with permission from ref. 88 and 90.

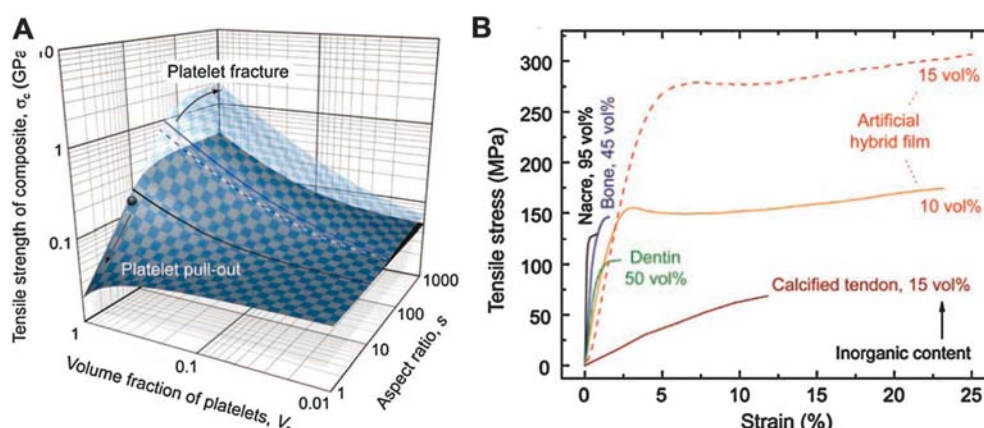


Fig. 15 (A) Estimated tensile strength of platelet-reinforced composites on the basis of a shear-lag model. The black and blue surfaces represent CaCO_3 /protein (nacre) and Al_2O_3 /chitosan composites, respectively. The black and blue full lines are the boundary between the platelet fracture and pull-out mode. Nacre is indicated with a black sphere. The Al_2O_3 platelet-reinforced composites with different platelet loading are shown with a blue dashed line. The strengths of protein, CaCO_3 platelets, chitosan and Al_2O_3 platelets are assumed to be 40, 400, 40 and 2000 MPa, respectively. (B) Comparison the mechanical properties of the artificial materials with those of natural materials. Adapted with permission from ref. 37.

natural materials (Fig. 15B). Most remarkably, the ultimate fracture strain was as high as 0.2, resulting from extensive plastic flow of chitosan. As a result, the work fracture of the artificial materials was more than one order of magnitude larger than that of nacre. However, low ceramic volume fraction resulted in an order of magnitude lower elastic modulus than nacre. After that, Yao *et al.*⁹³ fabricated a series of layered double hydroxides/chitosan nacre mimics using the same LBL bottom-up colloidal assembly. The highest tensile strength and Young's modulus for these hybrid films reached 160 MPa and 12.7 GPa, respectively. The strength improved by eight times compared with pure chitosan film and also followed the simple shear lag model.

2.4 Electrophoretic deposition

Electrophoresis deposition is a simple, inexpensive, and scalable technology and can rapidly produce films over large areas. Charged particles are forced to move toward the counter electrode (electrophoresis) and then coagulate on the electrode surface (deposition) under the application of external electric field (Fig. 16A).⁹⁴ It is also possible to create layered nanocomposites and realize complex material combinations.

Long *et al.*⁹⁵ prepared polyacrylamide/MTM nanocomposites by electrophoretic deposition of MTM in an aqueous suspension.

The MTMs were dispersed and modified with acrylamide monomers that were polymerized by ultraviolet radiation after deposition. The resulting film showed a layered structure with tens of nanometre thick MTM platelets as inorganic layers and polyacrylamide as interlayer phase. The inorganic content determined by thermogravimetric analysis was about 95.3 wt%, which was similar to that in nacre. The hardness and modulus of the film were 0.95 GPa and 16.92 GPa, respectively, which were higher than those of pure MTM film obtained by electrophoresis deposition. Subsequently, Wang *et al.*⁹⁶ used a hydrothermal method to intercalate an acrylic anodic electrophoretic resin into the interlayer space of MTM. After that, the polymer/MTM laminated structure was prepared by electrophoretic deposition. Prior to electrophoretic deposition, the thickness of the intercalated tactoids reduced from 23.4 to 11.3 nm and nanoindentation measurements indicated that the Young's modulus increased from 2.9 to 5.0 GPa. Liu *et al.*⁹⁷ arranged MTM tactoids into a layered arrangement by electrophoresis and found that the entrapment of nonplate particles caused by agglomeration of MTM deteriorated the layered structure.

Compared with LBL assembly, electrophoretic deposition produced layered polymer-MTM film with much lower mechanical properties. This is possibly attributed to the relatively

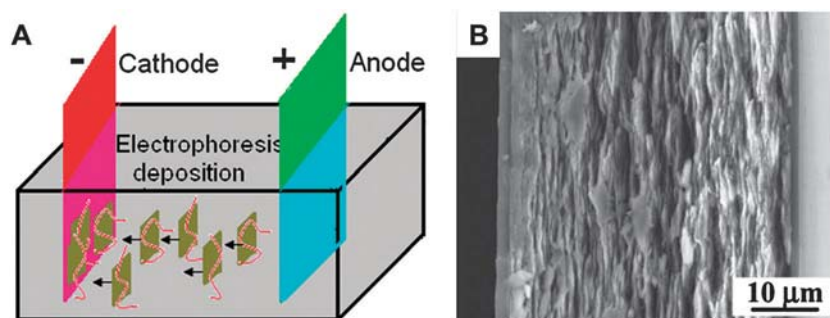


Fig. 16 (A) Schematic illustration of the assembly of positively charged nanoplatelets by electrophoretic deposition. (B) Cross-sectional SEM image of the gibbsite nanocomposite film. Adapted with permission from ref. 98.

poor alignment and a lack of optimum interface. In addition, it is important that the MTMs should be exfoliated fully as completely dispersed silicates rather than as the intercalated structures in the composite.

In a series of studies Lin *et al.*^{98–101} assembled gibbsite nanoplatelets into nacre-like structure by rapid electrodeposition technology. The gibbsite structure is a stacking of Al–OH layers, and each Al^{3+} is surrounded by six hydroxyl groups. It is positively charged in water, due to the reaction of surface hydroxyl groups with water and gibbsite nanoplatelets were modified with 3-(trimethoxysilyl)propyl methacrylate through silane coupling reaction, followed by electrophoretic deposition.⁹⁸ After the oriented assembly, the interstitials between the aligned nanoplatelets were filled with photocurable monomers and then polymerized, resulting in an optically transparent and strong layered thin film with 50 vol% inorganic platelets (Fig. 16B). The thickness of the film was controlled accurately by changing the concentration of colloidal gibbsite suspensions. The ceramic–polymer composite containing the unmodified gibbsite exhibited two-times higher tensile strength and three-times higher modulus than pure polymer films. Notably, a four-times higher tensile strength and one order of magnitude higher modulus than pure polymer were obtained for the composite prepared with the modified nanoplatelets. The tensile strength agreed with the calculated value according to eqn (5), indicating that composite failed under platelet pull-out mode. In order to increase the surface roughness to mimic the asperity of aragonite platelets found in nacre, a thin layer of sol–gel silica on smooth gibbsite nanoplatelets was prepared before electrophoretic deposition.⁹⁹ After electrodeposition, the interstitials between nanoplatelets were filled with the same matrix by photopolymerization. Interestingly, the tensile strain of the composites with rough nanoplatelets was five times higher than the composite with smooth platelets. The tensile strength increased slightly and the fracture work increased by six times.

In addition, the applied direct-current electric field also enables simultaneous assembly of positively charged gibbsite platelets and cationic polyelectrolytes (polyethylenimine) or non-ionic-type polymer (polyvinyl alcohol) between the inorganic nanosheets.^{100,101}

2.5 Mechanical assembly

To overcome some limitation in the techniques mentioned previously, several macroscopic mechanical processes including sedimentation, centrifugation, vacuum filtration, doctor blading,

slip casting and so on, have been developed to fabricate nacre-like materials. The general advantage of these methods is that thick films, even bulk materials, can be rapidly, economically produced for large-scale application.

Almqvist *et al.*¹⁰² first attempted to rapidly assemble talc tablets into nacre-like composites with high ceramic content by using different physical methods, including centrifugation, shearing cylinders, sedimentation, dipping, spinning cylinder, spinning plate and shearing plate. It was demonstrated that the effectiveness of the seven methods to align the tablets increased from centrifugation to shearing plates in the order shown in Fig. 17. Moreover, chemical surface treatment was in favor of orientation. More recently, Liu *et al.*⁹⁷ arranged smectite clay tactoids into layered arrangement without additives by five methods of sedimentation, centrifugation, slip casting, filtration and electrophoresis. It was found that slip casting method gave the best alignment. Le *et al.*¹⁰³ fabricated layered inorganic/organic nanocomposites with clay nanoplatelets and polyimide using a centrifugal deposition process in a short time (~ 15 min). The tensile strength and Young's modulus reached 80 MPa and 8 GPa, respectively, which were comparable to those of lamellar bones.

Aligned nacre-like MTM/PVA films were formed rapidly *via* paper-making (vacuum filtration), doctor-blading or simple painting by Walther *et al.*¹⁰⁴ The nacre-inspired paper had a Young's modulus of 27 GPa and a strength of 165 MPa, which partly surpassed those of nacre. A striking improvement of mechanical properties was obtained after the film was cross-linked using boric acid, a more powerful cross-linking agent compared with glutaraldehyde. The tensile modulus, ultimate stress and strain reached 50 GPa, 248 MPa and 0.9%, respectively. Compared to nacre the modulus was slightly lower, the strength was 2–3 fold higher, and the strain was similar. After that, MTM/PDDA films were prepared using the same physical method (Fig. 18A),¹⁰⁵ which possessed similar strength and modulus to that by LBL assembly.⁸⁵ Differently, the breakage of sacrificial bonds was not reflected in the stress–strain curve. Counterions of different valences could be uniformly introduced to the interfaces in MTM/PDDA film by infiltration (counterion exchange) (Fig. 18B). It was interesting that this created an interpenetrating network of counterions and thus tailored the interface strength. Increasing the charge of counterions led to improved strength and modulus (Fig. 18C). The most obvious improvements for strength and modulus were 151 MPa and 33 GPa, respectively,

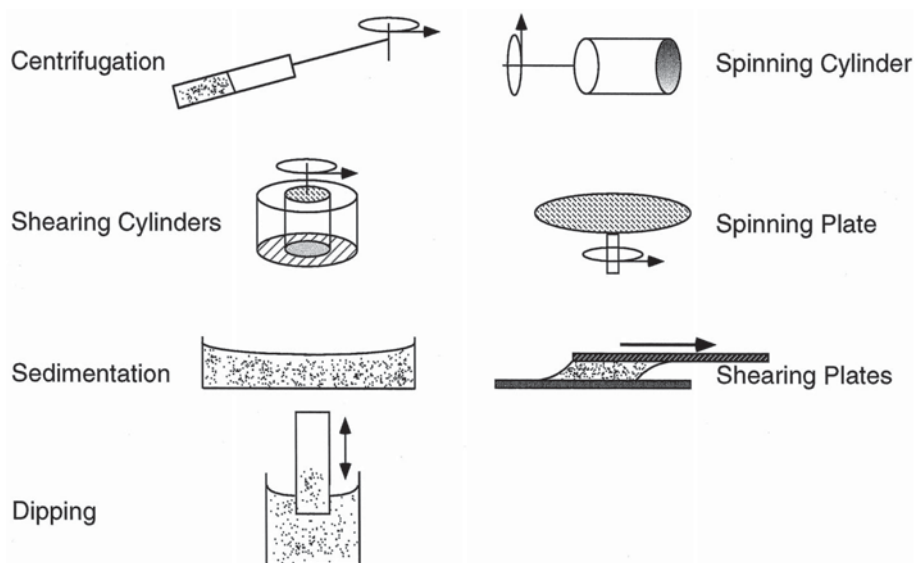


Fig. 17 Sketches of seven physical methods used to improve orientation of the talc tablets. Adapted with permission from ref. 102.

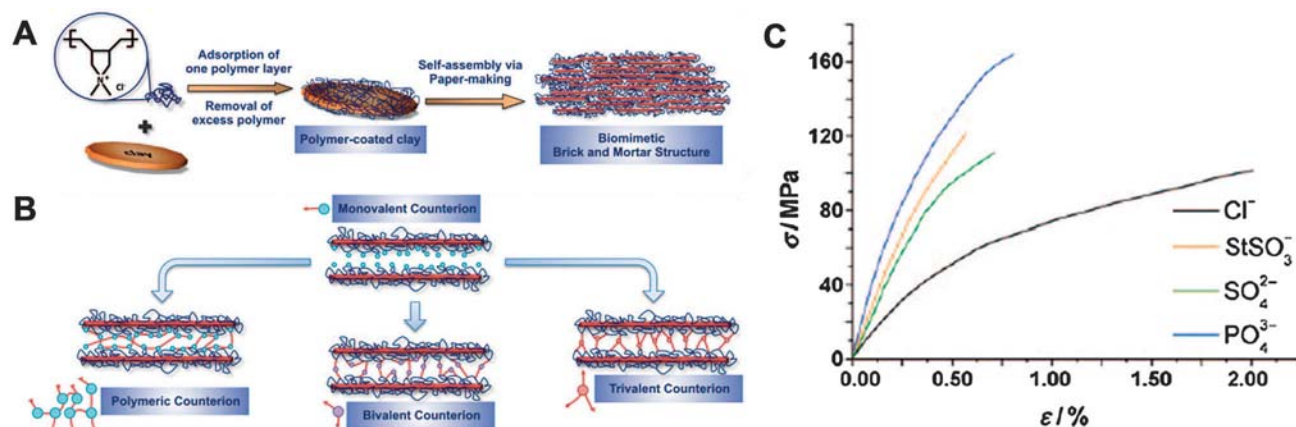


Fig. 18 (A) Preparation of brick-and-mortar structures with MTM and PDDA by paper-making method. (B) Supramolecular manipulation of the interaction between PDDA-coated MTM nanoplatelets by counterion exchange. The polymeric (StSO_3^-), bivalent (SO_4^{2-}) and trivalent (PO_4^{3-}) counterions are shown schematically on the left, middle and right, respectively. (C) Stress-strain curves of MTM/PDDA films before and after infiltration with counterions of different valences, showing increased tensile strength and modulus after counterion exchange. Adapted with permission from ref. 105.

after chlorine counterions was exchanged with PO_4^{3-} . The ultimate strain was comparable with nacre and reached 0.8%. Yao *et al.*⁹⁰ prepared artificial nacre-like MTM/chitosan films by vacuum filtration or evaporation. The mechanical properties were comparable with those by LBL assembly,⁸⁶ but was much lower than MTM/PVA film produced either by LBL assembly or vacuum filtration.^{88,104} The results of atomic modeling showed that the stereochemistry of the six rings in the chitosan molecules acted against formation of hydrogen bonds between MTM and chitosan (Fig. 14C). In addition, formation of Al–O–C bonds demonstrated in MTM/PVA LBL films⁸⁸ did not occur in MTM/chitosan composites, and were responsible for the lower mechanical properties.

Owing to its strong mechanical strength (fracture stress = $\sim 63 \text{ GPa}$ ¹⁰⁶) and unique two-dimensional sheet structure containing various oxygen functional groups, graphene oxide is a good candidate component for fabrication of the nacre-mimetic composites. Xu *et al.*¹⁰⁷ prepared graphene oxide/PVA composite

films simply by vacuum filtration of their aqueous solution. SEM images revealed a layered structure with oriented graphene oxide. Strong interfacial interaction was demonstrated by thermogravimetric analysis. The composite containing 3 wt% graphene oxide had 110 MPa tensile strength, 4.8 GPa modulus and 0.36% strain, where the modulus was much lower than for nacre, due to the low content of graphene oxide. Moreover, when the content of graphene oxide was more than 30%, the composite films showed brittle failure and a decrease of strength, probably resulting from the aggregation of graphene oxide sheets. Subsequently, Wang *et al.*¹⁰⁸ fabricated composite films of chitosan and reduced graphene oxide sheets with a layered structure by vacuum filtration. First, dispersed graphene oxide aqueous solution prepared *via* Hummer's method was stabilized by addition of a triblock copolymer before reduction. Afterwards, reduced graphene oxide sheet suspension was mixed with chitosan, followed by vacuum filtration. The tensile strength and modulus of the composite films increased dramatically when

incorporating the reduced graphene oxide with content in the range 1–6 wt%. The film with 6 wt% reduced graphene oxide exhibited 6.3 GPa modulus, 206 MPa tensile strength and 6.5% strain at rupture. Putz *et al.*¹⁰⁹ demonstrated highly ordered, homogeneous polymer nanocomposites of layered graphene oxide *via* vacuum filtration. The loading of graphene oxide could reach over 70 wt% in the composites. The obtained graphene oxide–PVA layered film had a Young's modulus of 36.4 GPa and tensile strength of 80.2 MPa. Another method for fabricating graphene oxide/polymer composites is solution mixing,^{110–113} however, due to the high van der Waals force, the graphene oxide nanosheets are easily aggregated in the polymer matrix, which results in random dispersion and lower loading of graphene oxide in the resultant composites. As a result, the mechanical properties are low, so to obtain the high performance composites based on graphene nanosheets, high graphene loading and well-assembled structure are required.

Submicron-thick glass flakes with silver coating were aligned by combining three-dimensional printing and hot press (Fig. 19A).¹¹⁴ Powders on the supply stage were carried to the building stage and aligned by a roller, and then bonded by PVA. Subsequently, the building stage was lowered for the next layer. The process was repeated many times to generate a green sample. Hot press was applied to further align and condense the stacked green samples. Bulky and dense glass/silver laminar composites containing over 80 vol% ceramic phase showed non-brittle fracture behavior due to interface delamination, crack deflection, and ligament bridging by the metal matrix, as shown in Fig. 19B. The work fracture was two orders of magnitude larger than for monolithic glasses.

Alumina flakes of comparable dimensions with aragonite platelets in nacre were aligned in epoxy matrix by hot-press assisted slip casting that combined hot pressing and slip casting.¹¹⁵ A bulk material with 60% volume fraction of ceramic phase, which could not be produced by direct mixing, displayed a clear brick-and-mortar structure. The composites had crack extension resistance by interface delamination and zigzagged crack deflection. The strength and modulus of the biomimetic composites were slightly higher than for a pristine epoxy and simple mix-process sample. However, the experimentally

determined modulus was much lower than the estimated values in terms of the rule of mixtures, due to poor interface bonding. Bonderer *et al.*^{116,117} used a combined gel-casting and hot-pressing method to fabricate alumina platelet-reinforced, extremely ductile thermoplastic polymer composites. Submicron-thick alumina platelets were dispersed in a highly diluted thermoplastic polymer solution. Upon cooling the casting suspension, polymer gel trapped the platelets in their well dispersed positions. Successive solvent evaporation induced strong shrinking in the height of the gel that promoted horizontal alignment of platelets. The plastic flow of melting polymers during hot-pressing further oriented the platelets. Instead of chitosan,³⁷ very ductile common polymers, polypropylene and polyurethane, were selected to pursue larger plastic deformation and higher platelets loading. The elastic modulus of the polyurethane composites with 53 vol% platelets was approximately 486 MPa, representing a 104-fold increase in stiffness compared with the pure polymer. It is interesting that the composite at platelets volume fraction as high as 33% deformed up to 162%. In addition, this method allows simple and rapid fabrication of polyurethane composites containing higher than 70 vol% platelets.

However, in contrast to alumina/chitosan hybrid materials,³⁷ the strength and modulus of polypropylene- and polyurethane-based composites were found to be greatly decreased. The strength, modulus and toughness of these composites as yet do not surpass those of nacre. These results indicate that selection of the mortar in a simple brick-and-mortar structure can only balance the strength and toughness in a limited range. To achieve excellent comprehensive properties requires a complex brick-and-mortar structure that can generate strain hardness. In other words, besides selection of the polymer partners with appropriate strength and ductility, a brick-and-mortar structure with waviness, rough platelets and inorganic bridges is necessary.

2.6 Chemical self-assembly

Besides the preformed inorganic building blocks, ceramic phases of layered organic–inorganic hybrid materials can be formed *in situ* from molecular precursors through mimicking the natural processing of nacre. Biomineralization takes place slowly at ambient temperature in aqueous environments from raw materials that widely exist in nature.¹¹⁸ As a template,

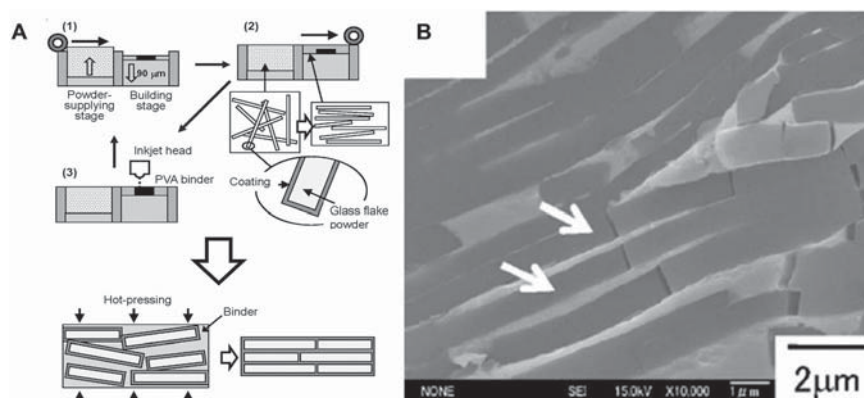


Fig. 19 (A) Scheme of a submicrometer-thick powder processing using a 3D printing machine and hot press. (B) Crack propagation behavior near Vickers indentation, showing interface delamination, crack deflection and ligament bridging (indicated by the white arrows). Adapted with permission from ref. 114.

organic components promote the formation and deposition, and control the nucleation, growth, organization and transformation of inorganic phases at the interface, through the complex interaction between organic and inorganic phases at the molecular level.¹¹⁹ Both self-assembly monolayers on substrates^{120–124} and Langmuir monolayers at air–solution interface,^{125–128} which provide synthetic surfaces for nucleation and growth, can be used to direct crystallization of inorganic phases, leading to single-phase films incorporating only one organic/inorganic interface. Furthermore, the Langmuir–Blodgett method is used to build lamellar heterostructures incorporating multiple organic/inorganic interfaces *via* repetitive depositions.^{129,130}

Supramolecular surfactant assemblies are used to form nanolaminate films. Such an approach can start with cast surfactant films followed by their infiltration with inorganic substances,^{131,132} or the surfactants and inorganic substances simultaneously assemble into the desired laminated structure in one processing step.¹³³ In the first route, a multilayer surfactant film was formed by casting an aqueous dispersion of dialkyl amphiphiles onto a substrate.¹³² The obtained film was dipped into a solution containing Cd^{2+} ions that intercalated into hydrophilic spaces, and then was exposed to hydrogen sulfide to produce CdS nanoparticles, leading to a layered heterostructure. The supramolecular assembly route to organic/inorganic nanolaminates in a single step was demonstrated by Brinker and co-workers *via* evaporation-induced self-assembly.^{134–139} The assembly process was based on evaporative dip-coating, spin-coating or casting processes and a evaporation-induced partitioning mechanism (Fig. 20A). It started from a homogeneous solution of soluble silicates, surfactant, organic monomers and initiators prepared in a volatile solvent–water mixture. The initial surfactant concentration was set below the critical micelle concentration (CMC). During coating, the surfactant concentration exceeded the CMC, due to preferential evaporation of the volatile solvent. As a result, organic

monomers and initiators were embedded into the hydrophobic micellar interiors and inorganic precursors were organized around the hydrophilic micellar exteriors. Further evaporation promoted co-assembly of the partitioned inorganic precursor–surfactant–monomer micellar species into a liquid-crystalline mesophase, resulting in formation of laminated silica/polymer composites in a very short time (Fig. 20B). The laminated mesostructure was maintained after polymerization of precursors and surfactant removal by washing (Fig. 20C and D). The selected surfactants as structure-directing agents included cationic, anionic, nonionic and block copolymers. In addition, this evaporation-induced self-assembly approach was also used to form polymer/indium-tin-oxide and polymer/titania nanolaminates.^{140–142} The mechanical properties and deformation behavior of these laminated composites fabricated by supramolecular assembly have not been reported.

Layered organic/inorganic composites with periodic microstructures were also obtained through combination of LBL assembly with chemical bath deposition (CBD) by Burghard *et al.*^{143–146} Organic layer deposition with a controllable thickness was performed by LBL assembly of oppositely charged polyelectrolytes. Preparation of inorganic layers was conducted by CBD, involving particle growth at surface nucleation sites of polyelectrolytes and simultaneous particle deposition from solution.¹⁴⁶ The thickness of inorganic layers was controlled by deposition time.¹⁴⁶ Sequential deposition of LBL organic layers and CBD inorganic layers led to multilayered structures, including TiO_2 /polyelectrolyte (Fig. 21A),^{143,145} ZnO /polyelectrolyte,¹⁴⁴ and ZrO_2 /polyelectrolyte.¹⁴⁶ It is interesting that the TiO_2 /polyelectrolyte heterolayer films possessed an increasing roughness compared with pure inorganic film, and had rippled interfaces between the inorganic and organic phases. The strong electrostatic attraction between the charged TiO_2 particles and adjacent oppositely-charged polyelectrolyte layer promoted partial interpenetration between layers, leading to TiO_2 bridges through

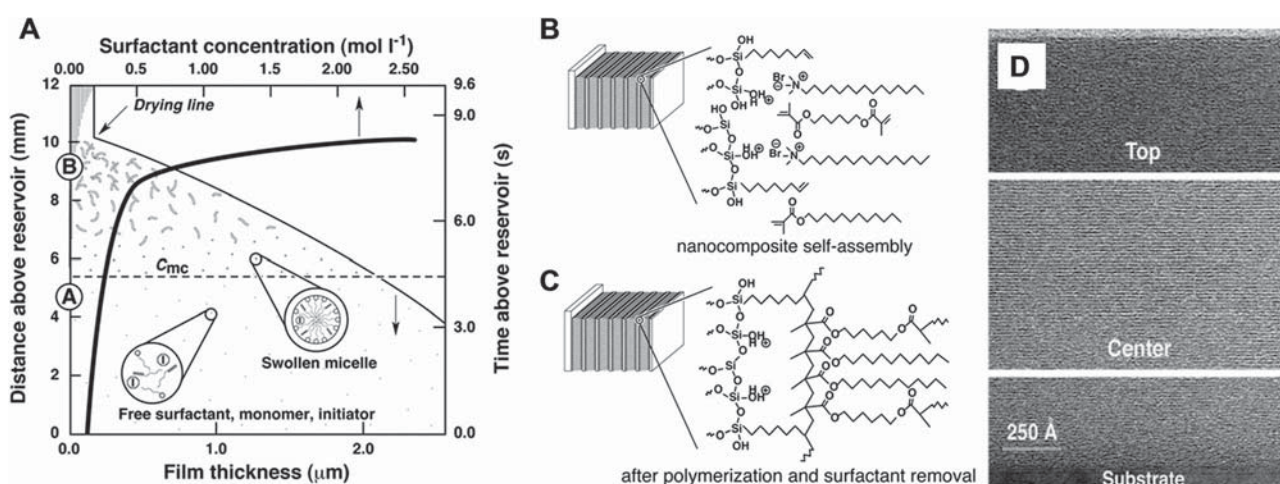


Fig. 20 (A) Diagrams showing evolution of nanolaminate structures during dip-coating. Evaporation induced micelle formation and concurrent incorporation of organic precursors into micellar interiors. Subsequently, the desired nanolaminated structure was formed through continued evaporation. (B) Hypothetical arrangement of surfactant, monomer, cross-linker and initiator adjacent to an oligomeric silica layer before polymerization. (C) Hypothetical structure of silica/poly(dodecylmethacrylate) nanocomposite after polymerization and surfactant removal by washing. (D) Representative TEM cross-section of ~ 500 nm thick nanocomposite film in the central region and regions adjacent to the substrate and vapor surfaces, showing *c*-axis oriented nanolaminate structure with successive layers. Adapted with permission from ref. 135.

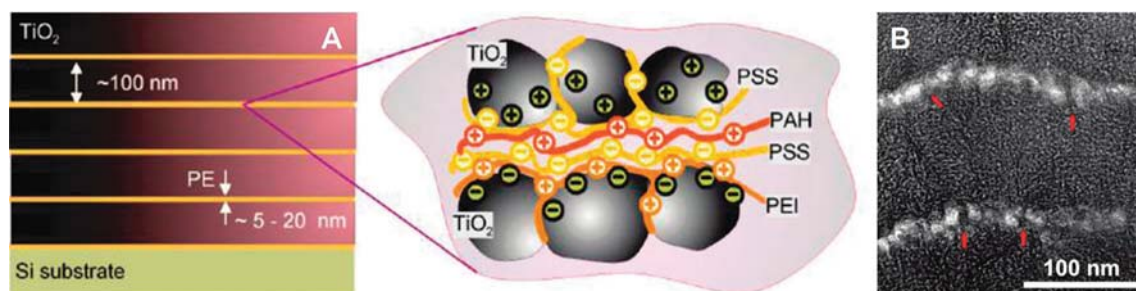


Fig. 21 (A) Cross-sectional structure of TiO_2 /polyelectrolyte hybrid films, prepared by alternate deposition of CBD TiO_2 layers and LBL polyelectrolyte layers. The thickness of polyelectrolyte and TiO_2 layers can be controlled by number of bilayers and time of CBD deposition, respectively. (B) High-resolution TEM images of the cross section of $(\text{polyelectrolyte}/\text{TiO}_2)_3$ hybrid film with a dark inorganic layer of ~ 100 nm thickness, and a bright organic layer of ~ 10 nm thickness. The red arrows mark TiO_2 bridges that penetrate through organic layers. Adapted with permission from ref. 145.

the polymer layers similar to aragonite bridges in nacre (Fig. 21B). Furthermore, the density of inorganic bridges could be modulated by the thickness of organic layers. The control over microstructure obviously facilitated the bioinspired thin films to reproduce features of nacre, generating optimal toughness, hardness and modulus.¹⁴⁵ However, there was a lack of interfacial contact between nanoscale TiO_2 particles in titania layers, in contrast to nanograins surrounded by viscoplastic biopolymer in nacre. Zhang *et al.*¹⁴⁷ prepared polyelectrolyte/ CaCO_3 multilayers by LBL self-assembly of diazo-resins and poly(acrylic acid), followed by growth of CaCO_3 crystals through CO_2 diffusion into the multilayers. Cross-linked LBL layers provided a negatively charged surface for promoting CaCO_3 nucleation. CO_2 diffusion method produced dense and uniform CaCO_3 strata with controllable thickness, which was hardly achieved by conventional immersion method. The artificial nacre with 93 wt% CaCO_3 was synthesized by adjusting the diffusion time of CO_2 and the number of LBL bilayers.

3. Conclusions and outlook

Much progress has been made in exploring multiscale and hierarchical structures, investigating the remarkable mechanical properties of nacre, and understanding of the relationship between them.¹⁴⁸ From the obtained knowledge on natural

nacre, six types of strategies have been successfully developed to fabricate artificial composites with layered structures and remarkable mechanical properties. Table 1 summarizes both advantages and disadvantages of all the preparation methods.

However, there are still many challenges that need to be addressed. First, the synergy of factors acting over multiple scales to toughness should be clearly elucidated. Second, the manufacture of man-made composites that copy nacre's multiscale fine features, such as platelet waviness, mineral bridges and nanoasperities, remains a great challenge.

A fundamental principle of materials science is that the mechanical properties of composites are determined by their composition, structure and interface. Different from biomaterials, artificial materials can be synthesized with much stronger building blocks (alumina, MTM, graphene, *etc.*) instead of biominerals (CaCO_3). All types of natural and synthetic polymers can also be used to tailor the interface properties. Some artificial hybrid films indeed come to the top in tensile strength. However, brittle fracture occurs for these films, leading to lower ultimate strain than nacre (Table 2). The improved toughness, an important parameter for bulk ceramic materials, is, as yet, not as outstanding as for nacre (Fig. 22). It is suggested that the simple brick-and-mortar structure and tailoring interface are insufficient for excellent combination of modulus, strength and toughness. The striking toughness of nacre is not achieved only by its

Table 1 Comparison of six strategies to fabricate nacre-inspired layered composites

Synthesis strategies	Advantages	Disadvantages
Conventional method for bulk ceramic materials Freezing casting	<ul style="list-style-type: none"> Simple, easily scaled up For bulk materials Bulk materials with high toughness 	<ul style="list-style-type: none"> Layer with large thickness (> 100 μm) Less prominent improvement of the toughness Energy-consuming during freezing and sintering Low volume fraction of ceramic phase compared with nacre
Layer-by-layer deposition	<ul style="list-style-type: none"> Thin layer (several micrometre) Control of nanometre structure Precise control of interface thickness Fine control over layered structure High loading of inorganic phase 	<ul style="list-style-type: none"> Time-consuming Difficult to be scaled up
Electrophoretic deposition	<ul style="list-style-type: none"> Simple, inexpensive and scalable technology for fabricating large area film 	<ul style="list-style-type: none"> Low mechanical properties of the layered composites
Mechanical assembly	<ul style="list-style-type: none"> Fast, economical, large-scale fabrication 	<ul style="list-style-type: none"> Difficult to control the layered structure at nanometre level
Chemical self-assembly	<ul style="list-style-type: none"> Film, and bulk layered materials Assembly of layered materials at molecular level 	<ul style="list-style-type: none"> Difficult to fabricate large-scale layered composites

Table 2 Tensile strength, Young's modulus and strain of nacre compared with some nacre-like layered films. As yet, the integrated mechanical properties for the synthetic films do not surpass those of nacre

Synthesis strategy	Layered composite	Inorganic loading	Tensile strength/MPa	Young's modulus/GPa	Strain (%)	Year ^{Ref.}
Biomimetalization	Nacre	95 vol%	80–135	60–70	0.9	1988 ¹
LBL	PDDA/MTM	30 vol%	106 ± 11	11 ± 2	8.4	2003 ⁸⁵
LBL	Chitosan/MTM	42 vol%	81 ± 12	6.1 ± 0.8	1.9	2007 ⁸⁶
LBL	DOPA-based MTM + Fe ³⁺	65 wt%	200 ± 28	6.8 ± 0.9	3.8	2007 ⁸⁷
LBL	PVA/MTM	50 vol%	150 ± 40	13 ± 2	0.7	2007 ⁸⁸
LBL	PVA/MTM + GA	50 vol%	400 ± 40	106 ± 11	0.33	2007 ⁸⁸
LBL	PVA/MTM + Al ³⁺	50 vol%	250 ± 50	41 ± 5	0.33	2008 ⁸⁹
LBL	PVA/MTM + Cu ²⁺	50 vol%	320 ± 40	58 ± 6	0.28	2008 ⁸⁹
LBL	Chitosan/Al ₂ O ₃ platelets	15 vol%	315 ± 95	9.6 ± 2	21	2008 ³⁷
Electrophoretic deposition	Gibbsite/silane	50 vol%	55	5.4	1.2	2009 ⁹⁸
Vacuum filtration	PVA/GO	2.5 vol%	110 ± 7	4.8 ± 0.3	36	2009 ¹⁰⁸
Vacuum filtration	Chitosan/GO	6 wt%	206 ± 6	6.3 ± 0.2	6.5	2010 ¹¹⁴
Vacuum filtration	MTM/chitosan	70 wt%	76	10.7	0.97	2010 ⁹⁰
Vacuum filtration	PVA/MTM + borate	50 vol%	248 ± 19	45.6 ± 3.9	0.9	2010 ¹⁰⁴
Vacuum filtration	MTM/PDDA + PO ₄ ³⁻	70 wt%	151	32.9	0.8	2010 ¹⁰⁵
Gel-casting and hot-pressing	TPU/Al ₂ O ₃ platelets	43 vol%	15	0.486	40	2010 ¹¹⁷

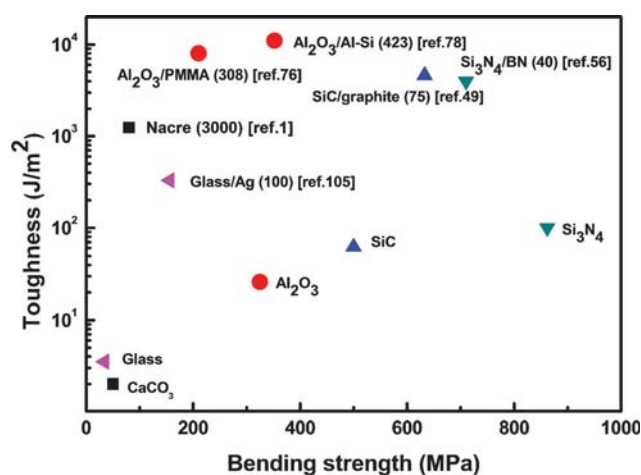


Fig. 22 Fracture toughness vs. bending strength of nacre compared with some layered ceramic materials. Improved times of toughness in comparison with monolithic ceramics is given in parentheses. The corresponding literatures are presented in square brackets.

composition (viscoelastic biopolymer glue), but also by accurately designing microstructure at multiple scales. The ability to replicate its unique structure and generate strain hardening is desirable. Only in this way can maximum activation of all the potential plastic deformation regions between the layers at failure be realised, so leading to the largest energy dissipation. Fabrication of biomimetic nacre materials with outstanding integrated mechanical properties needs to be further optimized *via* selection of suitable inorganic phases, accurate design **and control over the segmented layered structure at distinct length levels, with reasonable interface and high ceramic content.**

The efficient processing of ordered structures at multiscale levels remains a goal in the future. A higher degree of alignment by rapid assembly including both physical and chemical methods is needed. **In addition, the optimised aragonite-biopolymer interface should be targeted at two hierarchical levels, by increasing the interfacial area which contributes to enhanced toughness. It can be anticipated that artificial composites will dramatically benefit from this two-level hierarchical structure.**

Acknowledgements

This work was supported by the National Research Fund for Fundamental Key Projects (2011CB935700, 2010CB934700, 2009CB930404, 2009CB930401, 2007CB936403), the Fundamental Research Funds for the Central Universities (YWF-10-02-052, YWF-10-01-B16), the Research Fund for the Doctoral Program of Higher Education (20101102120044 and 20101102110035), the National Natural Science Foundation (51103004, 21003132, 20920102036, 209774113), the National Natural Science Foundation for Distinguished Youth Scholars of China (21025310), the 100-Talent Program of Chinese Academy of Sciences, and the National Science Foundation of China (20973047), and the Scientific Research Foundation for the Returned Overseas Chinese Scholars, State Education Ministry, P. R. China.

References

- 1 A. Jackson, J. Vincent and R. Turner, *Proc. R. Soc. London, Ser. B*, 1988, **234**, 415–440.
- 2 M. Sarikaya, *Microsc. Res. Tech.*, 1994, **27**, 360–375.
- 3 G. Mayer, *Science*, 2005, **310**, 1144–1147.
- 4 M. A. Meyers, P. Y. Chen, A. Y. M. Lin and Y. Seki, *Prog. Mater. Sci.*, 2008, **53**, 1–206.
- 5 M. Sarikaya and I. A. Aksay, *Storming Media*, 1995.
- 6 U. G. K. Wegst and M. F. Ashby, *Philos. Mag.*, 2004, **84**, 2167–2181.
- 7 C. Grégoire, *J. Cell Biol.*, 1957, **3**, 797–808.
- 8 N. Watabe, *J. Ultrastruct. Res.*, 1965, **12**, 351–370.
- 9 K. Wada, *Bull. Nat. Pearl. Res. Lab.*, 1961, **7**, 703–828.
- 10 K. Wada, *Bull. Nat. Pearl. Res. Lab.*, 1968, **13**, 1561–1596.
- 11 S. W. Wise, *Eclogae. Geol. Helv.*, 1970, **63**, 775–797.
- 12 M. Omori and N. Watabe, *Proceedings of the Third International Biomimetalization Symposium 1980*, Tokai University Press in Tokyo, Japan.
- 13 F. Barthelat, H. Tang, P. Zavattieri, C. M. Li and H. Espinosa, *J. Mech. Phys. Solids*, 2007, **55**, 306–337.
- 14 S. Blank, M. Arnoldi, S. Khoshnavaz, L. Treccani, M. Kuntz, K. Mann, G. Grathwohl and M. Fritz, *J. Microsc.*, 2003, **212**, 280–291.
- 15 Q. Feng, F. Cui, G. Pu, R. Wang and H. Li, *Mater. Sci. Eng., C*, 2000, **11**, 19–25.
- 16 S. Manne, C. Zaremba, R. Giles, L. Huggins, D. Walters, A. Belcher, D. Morse, G. Stucky, J. Didymus and S. Mann, *Proc. R. Soc. London, Ser. B*, 1994, **256**, 17–23.

- 17 B. Bruet, H. Qi, M. Boyce, R. Panas, K. Tai, L. Frick and C. Ortiz, *J. Mater. Res.*, 2011, **20**, 2400–2419.
- 18 F. Barthelat, C. M. Li, C. Comi and H. D. Espinosa, *J. Mater. Res.*, 2011, **21**, 1977–1986.
- 19 A. Y. M. Lin, P. Y. Chen and M. A. Meyers, *Acta Biomater.*, 2008, **4**, 131–138.
- 20 R. Z. Wang, Z. Suo, A. G. Evans, N. Yao and I. A. Aksay, *J. Mater. Res.*, 2011, **16**, 2485–2493.
- 21 X. Li, W. C. Chang, Y. J. Chao, R. Wang and M. Chang, *Nano Lett.*, 2004, **4**, 613–617.
- 22 X. Li, Z. H. Xu and R. Wang, *Nano Lett.*, 2006, **6**, 2301–2304.
- 23 H. D. Espinosa, J. E. Rim, F. Barthelat and M. J. Buehler, *Prog. Mater. Sci.*, 2009, **54**, 1059–1100.
- 24 J. Currey, *Proc. R. Soc. London, Ser. B*, 1977, **196**, 443–463.
- 25 F. Barthelat and H. Espinosa, *Exp. Mech.*, 2007, **47**, 311–324.
- 26 R. Menig, M. Meyers, M. Meyers and K. Vecchio, *Acta Mater.*, 2000, **48**, 2383–2398.
- 27 F. Barthelat and H. D. Espinosa, *Mech. Prop. Bioinspired Biol. Mater.*, 2005, **844**, 67–78.
- 28 B. Mohanty, K. S. Katti and D. R. Katti, *Mech. Res. Commun.*, 2008, **35**, 17–23.
- 29 B. L. Smith, T. E. Schaffer, M. Viani, J. B. Thompson, N. A. Frederick, J. Kindt, A. Belcher, G. D. Stucky, D. E. Morse and P. K. Hansma, *Nature*, 1999, **399**, 761–763.
- 30 F. Song, J. Zhou, X. Xu, Y. Xu and Y. Bai, *Phys. Rev. Lett.*, 2008, **100**, 245502.
- 31 H. Wagner and S. Weiner, *J. Biomech.*, 1992, **25**, 1311–1320.
- 32 I. J. Ger and P. Fratzl, *Biophys. J.*, 2000, **79**, 1737–1746.
- 33 A. G. Evans, Z. Suo, R. Z. Wang, I. A. Aksay, M. Y. He and J. W. Hutchinson, *J. Mater. Res.*, 2011, **16**, 2475–2484.
- 34 F. Song, X. H. Zhang and Y. L. Bai, *J. Mater. Res.*, 2011, **17**, 1567–1570.
- 35 F. Song, A. Soh and Y. Bai, *Biomaterials*, 2003, **24**, 3623–3631.
- 36 M. A. Meyers, A. Y. M. Lin, P. Y. Chen and J. Muiyco, *J. Mech. Behav. Biomed. Mater.*, 2008, **1**, 76–85.
- 37 A. R. Studart, L. J. Bonderer and L. J. Gauckler, *Science*, 2008, **319**, 1069–1073.
- 38 P. K. V. V. Nukala and S. Simunovic, *Biomaterials*, 2005, **26**, 6087–6098.
- 39 M. Sarikaya, K. E. Gunnison, M. Yasrebi and I. A. Aksay, *MRS Online Proc. Libr.*, 2011, **174**, 109–116.
- 40 G. Mayer and M. Sarikaya, *Exp. Mech.*, 2002, **42**, 395–403.
- 41 R. Wang, H. Wen, F. Cui, H. Zhang and H. Li, *J. Mater. Sci.*, 1995, **30**, 2299–2304.
- 42 F. Song and Y. Bai, *J. Mater. Res.*, 2011, **18**, 1741–1744.
- 43 B. R. Lawn, *Fracture of Brittle Solids*, Cambridge University Press, 1993.
- 44 R. Rabiei, S. Bekah and F. Barthelat, *Acta Biomater.*, 2010, **6**, 4081–4089.
- 45 J. B. Thompson, J. H. Kindt, B. Drake, H. G. Hansma, D. E. Morse and P. K. Hansma, *Nature*, 2001, **414**, 773–776.
- 46 G. E. Fantner, T. Hassenkam, J. H. Kindt, J. C. Weaver, H. Birkedal, L. Pechenik, J. A. Cutroni, G. A. G. Cidade, G. D. Stucky and D. E. Morse, *Nat. Mater.*, 2005, **4**, 612–616.
- 47 T. E. Schaffer, C. Ionescu-Zanetti, R. Proksch, M. Fritz, D. A. Walters, N. Almqvist, C. M. Zaremba, A. M. Belcher, B. L. Smith and G. D. Stucky, *Chem. Mater.*, 1997, **9**, 1731–1740.
- 48 M. Sarikaya and I. A. Aksay, in *Structure, Cellular Synthesis and Assembly of Biopolymers*, ed. S. T. Case, Springer-Verlag, Amsterdam, 1992, pp. 1–25.
- 49 W. J. Clegg, K. Kendall, N. M. Alford, T. W. Button and J. D. Birchall, *Nature*, 1990, **347**, 455–457.
- 50 B. Chen, X. Peng, J. Wang and X. Wu, *Ceram. Int.*, 2004, **30**, 2011–2014.
- 51 S. Zhao, J. Zhang, W. Li and H. Li, *Compos. Sci. Technol.*, 2003, **63**, 1009–1014.
- 52 L. Zhang and V. Krstic, *Theor. Appl. Fracture Mech.*, 1995, **24**, 13–19.
- 53 D. Kovar, M. Thouless and J. W. Halloran, *J. Am. Ceram. Soc.*, 2005, **81**, 1004–1112.
- 54 Z. Lences, K. Hirao, M. E. Brito, M. Toriyama and S. Kanzaki, *J. Am. Ceram. Soc.*, 2004, **83**, 2503–2508.
- 55 C. A. Wang, Y. Huang, Q. F. Zan, H. Guo and S. Y. Cai, *Mater. Sci. Eng., C*, 2000, **11**, 9–12.
- 56 C. Wang, Y. Huang, Q. Zan, L. Zou and S. Cai, *J. Am. Ceram. Soc.*, 2002, **85**, 2457–2461.
- 57 L. Zou, Y. Huang, R. Chen, C. A. Wang and D. S. Park, *J. Eur. Ceram. Soc.*, 2003, **23**, 1987–1996.
- 58 L. Zou, Y. Huang and C. Wang, *J. Eur. Ceram. Soc.*, 2004, **24**, 2861–2868.
- 59 X. D. Li, L. H. Zou, H. Ni, A. R. Reynolds, C. A. Wang and Y. Huang, *Mater. Sci. Eng., C*, 2008, **28**, 1501–1508.
- 60 T. Ohji, Y. Shigegaki, T. Miyajima and S. Kanzaki, *J. Am. Ceram. Soc.*, 2005, **80**, 991–994.
- 61 K. Blanks, A. Kristoffersson, E. Carlström and W. Clegg, *J. Eur. Ceram. Soc.*, 1998, **18**, 1945–1951.
- 62 J. Requena, R. Moreno and J. S. Moya, *J. Am. Ceram. Soc.*, 1989, **72**, 1511–1513.
- 63 D. B. Marshall, J. J. Ratto and F. F. Lange, *J. Am. Ceram. Soc.*, 1991, **74**, 2979–2987.
- 64 P. Sarkar, X. Haung and P. S. Nicholson, *J. Am. Ceram. Soc.*, 1992, **75**, 2907–2909.
- 65 K. P. Plucknett, C. H. Caceres, C. Hughes and D. S. Wilkinson, *J. Am. Ceram. Soc.*, 1994, **77**, 2145–2153.
- 66 T. Chartier, D. Merle and J. Besson, *J. Eur. Ceram. Soc.*, 1995, **15**, 101–107.
- 67 E. Lucchini and O. Sbaizero, *J. Eur. Ceram. Soc.*, 1995, **15**, 975–981.
- 68 C. J. Russo, M. P. Harmer, H. M. Chan and G. A. Miller, *J. Am. Ceram. Soc.*, 1992, **75**, 3396–3400.
- 69 H. Katsuki and Y. Hirata, *J. Ceram. Soc. Jpn.*, 1990, **98**, 1114–1119.
- 70 N. P. Padture, D. C. Pender, S. Wuttiphon and B. R. Lawn, *J. Am. Ceram. Soc.*, 1995, **78**, 3160–3162.
- 71 H. Y. Liu, B. R. Lawn and S. M. Hsu, *J. Am. Ceram. Soc.*, 1996, **79**, 1009–1014.
- 72 W. J. Clegg, *Acta Metall. Mater.*, 1992, **40**, 3085–3093.
- 73 G. Mayer, *Mater. Sci. Eng., C*, 2006, **26**, 1261–1268.
- 74 H. D. Espinosa, A. L. Juster, F. J. Latourte, O. Y. Loh, D. Gregoire and P. D. Zavattieri, *Nat. Commun.*, 2011, **2**, 173.
- 75 S. Deville, E. Saiz, R. K. Nalla and A. P. Tomsia, *Science*, 2006, **311**, 515.
- 76 E. Munch, M. E. Launey, D. H. Alsem, E. Saiz, A. P. Tomsia and R. O. Ritchie, *Science*, 2008, **322**, 1516.
- 77 M. E. Launey, E. Munch, D. H. Alsem, H. Barth, E. Saiz, A. P. Tomsia and R. O. Ritchie, *Acta Mater.*, 2009, **57**, 2919–2932.
- 78 M. E. Launey, E. Munch, D. H. Alsem, E. Saiz, A. P. Tomsia and R. O. Ritchie, *J. R. Soc. Interface*, 2009, **7**, 741–753.
- 79 O. L. Manevitch and G. C. Rutledge, *J. Phys. Chem. B*, 2004, **108**, 1428–1435.
- 80 P. B. Messersmith and E. P. Giannelis, *Chem. Mater.*, 1994, **6**, 1719–1725.
- 81 J. Rexer and E. Anderson, *Polym. Eng. Sci.*, 1979, **19**, 1–11.
- 82 D. Schmidt, D. Shah and E. P. Giannelis, *Curr. Opin. Solid State Mater. Sci.*, 2002, **6**, 205–212.
- 83 E. R. Klinefeld and G. S. Ferguson, *Science*, 1994, **265**, 370.
- 84 N. A. Kotov, T. Haraszti, L. Turi, G. Zavala, R. E. Geer, I. Dekany and J. H. Fendler, *J. Am. Chem. Soc.*, 1997, **119**, 6821–6832.
- 85 Z. Tang, N. A. Kotov, S. Magonov and B. Ozturk, *Nat. Mater.*, 2003, **2**, 413–418.
- 86 P. Podsiadlo, Z. Y. Tang, B. S. Shim and N. A. Kotov, *Nano Lett.*, 2007, **7**, 1224–1231.
- 87 P. Podsiadlo, Z. Q. Liu, D. Paterson, P. B. Messersmith and N. A. Kotov, *Adv. Mater.*, 2007, **19**, 949–955.
- 88 P. Podsiadlo, A. K. Kaushik, E. M. Arruda, A. M. Waas, B. S. Shim, J. D. Xu, H. Nandivada, B. G. Pumplun, J. Lahann, A. Ramamoorthy and N. A. Kotov, *Science*, 2007, **318**, 80–83.
- 89 P. Podsiadlo, A. K. Kaushik, B. S. Shim, A. Agarwal, Z. Y. Tang, A. M. Waas, E. M. Arruda and N. A. Kotov, *J. Phys. Chem. B*, 2008, **112**, 14359–14363.
- 90 H. B. Yao, Z. H. Tan, H. Y. Fang and S. H. Yu, *Angew. Chem., Int. Ed.*, 2010, **49**, 10127–10131.
- 91 P. Podsiadlo, M. Michel, J. Lee, E. Verploegen, N. W. S. Kam, V. Ball, Y. Qi, A. J. Hart, P. T. Hammond and N. A. Kotov, *Nano Lett.*, 2008, **8**, 1762–1770.
- 92 V. Vertlib, M. Dietiker, M. Plotze, L. Yezek, R. Spolenak and A. M. Puzrin, *J. Mater. Res.*, 2011, **23**, 1026–1035.
- 93 H. B. Yao, H. Y. Fang, Z. H. Tan, L. H. Wu and S. H. Yu, *Angew. Chem., Int. Ed.*, 2010, **49**, 2140–2145.

- 94 I. Zhitomirsky, *Adv. Colloid Interface Sci.*, 2002, **97**, 279–315.
- 95 B. Long, C. A. Wang, W. Lin, Y. Huang and J. Sun, *Compos. Sci. Technol.*, 2007, **67**, 2770–2774.
- 96 C. A. Wang, W. Lin, H. L. Le, B. Long and Y. Huang, *Mater. Sci. Eng., C*, 2008, **28**, 1031–1037.
- 97 T. Liu, B. Chen and J. R. G. Evans, *Bioinspir. Biomimetics*, 2008, **3**, 016005.
- 98 T. H. Lin, W. H. Huang, I. K. Jun and P. Jiang, *Chem. Mater.*, 2009, **21**, 2039–2044.
- 99 T. H. Lin, W. H. Huang, I. K. Jun and P. Jiang, *J. Colloid Interface Sci.*, 2010, **344**, 272–278.
- 100 T. H. Lin, W. H. Huang, I. K. Jun and P. Jiang, *Electrochem. Commun.*, 2009, **11**, 14–17.
- 101 T. H. Lin, W. H. Huang, I. K. Jun and P. Jiang, *Electrochem. Commun.*, 2009, **11**, 1635–1638.
- 102 N. Almqvist, N. H. Thomson, B. L. Smith, G. D. Stucky, D. E. Morse and P. K. Hansma, *Mater. Sci. Eng., C*, 1999, **7**, 37–43.
- 103 H. R. Le, R. F. Chen, C. A. Wang and Y. Huang, *Mater. Sci. Eng., C*, 2008, **28**, 218–222.
- 104 A. Walther, I. Bjurhager, J. M. Malho, J. Pere, J. Ruokolainen, L. A. Berglund and O. Ikkala, *Nano Lett.*, 2010, **10**, 2742–2748.
- 105 A. Walther, I. Bjurhager, J. M. Malho, J. Ruokolainen, L. Berglund and O. Ikkala, *Angew. Chem., Int. Ed.*, 2010, **49**, 6448–6453.
- 106 J. T. Paci, T. Belytschko and G. C. Schatz, *J. Phys. Chem. C*, 2007, **111**, 18099–18111.
- 107 Y. Xu, W. Hong, H. Bai, C. Li and G. Shi, *Carbon*, 2009, **47**, 3538–3543.
- 108 X. L. Wang, H. Bai, Z. Y. Yao, A. R. Liu and G. Q. Shi, *J. Mater. Chem.*, 2010, **20**, 9032–9036.
- 109 K. W. Putz, O. C. Compton, M. J. Palmeri, S. T. Nguyen and L. C. Brinson, *Adv. Funct. Mater.*, 2010, **20**, 3322–3329.
- 110 S. Stankovich, D. A. Dikin, G. H. B. Dommett, K. M. Kohlhaas, E. J. Zimney, E. A. Stach, R. D. Piner, S. T. Nguyen and R. S. Ruoff, *Nature*, 2006, **442**, 282–286.
- 111 X. Zhao, Q. H. Zhang, D. J. Chen and P. Lu, *Macromolecules*, 2010, **43**, 2357–2363.
- 112 X. Yang, Y. Tu, L. Li, S. Shang and X.-m. Tao, *ACS Appl. Mater. Interfaces*, 2010, **2**, 1707–1713.
- 113 E. Tkalya, M. Ghislandi, A. Alekseev, C. Koning and J. Loos, *J. Mater. Chem.*, 2010, **20**, 3035–3039.
- 114 H. Kakisawa, T. Sumitomo, R. Inoue and Y. Kagawa, *Compos. Sci. Technol.*, 2010, **70**, 161–166.
- 115 H. Kakisawa, O. O. Ekiz and A. F. Dericioglu, *Mater. Sci. Eng. C: Mater. Biol. Appl.*, 2009, **29**, 2050–2054.
- 116 L. J. Bonderer, K. Feldman and L. J. Gauckler, *Compos. Sci. Technol.*, 2010, **70**, 1958–1965.
- 117 L. J. Bonderer, K. Feldman and L. J. Gauckler, *Compos. Sci. Technol.*, 2010, **70**, 1966–1972.
- 118 V. C. Sundar, A. D. Yablon, J. L. Grazul, M. Ilan and J. Aizenberg, *Nature*, 2003, **424**, 899–900.
- 119 S. Mann, *Nature*, 1993, **365**, 499–505.
- 120 A. Heuer, D. Fink, V. Laraia, J. Arias, P. Calvert, K. Kendall, G. Messing, J. Blackwell, P. Rieke and D. Thompson, *Science*, 1992, **255**, 1098–1105.
- 121 B. Bunker, P. Rieke, B. Tarasevich, A. Campbell, G. Fryxell, G. Graff, L. Song, J. Liu, J. Virden and G. McVay, *Science*, 1994, **264**, 48–55.
- 122 B. J. Tarasevich, P. C. Rieke and J. Liu, *Chem. Mater.*, 1996, **8**, 292–300.
- 123 H. Pizem and C. N. Sukenik, *Chem. Mater.*, 2002, **14**, 2476–2485.
- 124 T. M. Fuchs, R. C. Hoffmann, T. P. Niesen, H. Tew, J. Bill and F. Aldinger, *J. Mater. Chem.*, 2002, **12**, 1597–1601.
- 125 B. R. Heywood and S. Mann, *Adv. Mater.*, 1994, **6**, 9–20.
- 126 S. Rajam, B. R. Heywood, J. B. A. Walker, S. Mann, R. J. Davey and J. D. Birchall, *J. Chem. Soc., Faraday Trans.*, 1991, **87**, 727–734.
- 127 B. R. Heywood, S. Rajam and S. Mann, *J. Chem. Soc., Faraday Trans.*, 1991, **87**, 735–743.
- 128 B. R. Heywood and S. Mann, *Chem. Mater.*, 1994, **6**, 311–318.
- 129 T. Yamaki and K. Asai, *Langmuir*, 2001, **17**, 2564–2567.
- 130 H. Gong, M. Pluntke, O. Marti, P. Walther, L. Gower, H. Cölfen and D. Volkmer, *Colloids Surf., A*, 2010, **354**, 279–283.
- 131 I. Ichinose, N. Kimizuka and T. Kunitake, *J. Phys. Chem.*, 1995, **99**, 3736–3742.
- 132 P. Osenar, P. V. Braun and S. I. Stupp, *Adv. Mater.*, 1996, **8**, 1022–1025.
- 133 I. A. Aksay, M. Trau, S. Manne, I. Honma, N. Yao, L. Zhou, P. Fenter, P. M. Eisenberger and S. M. Gruner, *Science*, 1996, **273**, 892–898.
- 134 Y. Lu, Y. Yang, A. Sellinger, M. Lu, J. Huang, H. Fan, R. Haddad, G. Lopez, A. R. Burns and D. Y. Sasaki, *Nature*, 2001, **410**, 913–917.
- 135 A. Sellinger, P. M. Weiss, A. Nguyen, Y. Lu, R. A. Assink, W. Gong and C. J. Brinker, *Nature*, 1998, **394**, 256–260.
- 136 Y. F. Lu, H. Y. Fan, N. Doke, D. A. Loy, R. A. Assink, D. A. LaVan and C. J. Brinker, *J. Am. Chem. Soc.*, 2000, **122**, 5258–5261.
- 137 B. Smarsly, G. Garnweitner, R. Assink and C. J. Brinker, *Prog. Org. Coat.*, 2003, **47**, 393–400.
- 138 M. H. Huang, H. M. Soye, B. S. Dunn, J. I. Zink, A. Sellinger and C. J. Brinker, *J. Sol-Gel Sci. Technol.*, 2008, **47**, 300–310.
- 139 C. J. Brinker, Y. Lu, A. Sellinger and H. Fan, *Adv. Mater.*, 1999, **11**, 579–585.
- 140 S. Zhang, B. He, Z. Zhang, H. Dang, W. Liu and Q. Xue, *Chem. Lett.*, 2004, **33**, 1498–1499.
- 141 X. Zhang, C. Liu, W. Wu and J. Wang, *Mater. Lett.*, 2006, **60**, 2086–2089.
- 142 S. M. Zhang, Y. J. Gao, Z. J. Zhang, H. X. Dang, W. M. Liu and Q. J. Xue, *Acta Chim. Sinica*, 2002, **60**, 1497–1501.
- 143 Z. Burghard, A. Tucic, L. P. H. Jeurgens, R. C. Hoffmann, J. Bill and F. Aldinger, *Adv. Mater.*, 2007, **19**, 970–974.
- 144 P. Lipowsky, Burghard, L. P. H. Jeurgens, J. Bill and F. Aldinger, *Nanotechnology*, 2007, **18**, 345707.
- 145 Z. Burghard, L. Zini, V. Srot, P. Bellina, P. A. Aken and J. Bill, *Nano Lett.*, 2009, **9**, 4103–4108.
- 146 I. Zlotnikov, I. Gotman, Z. Burghard, J. Bill and E. Y. Gutmanas, *Colloids Surf., A*, 2010, **361**, 138–142.
- 147 X. Zhang, H. Wei, N. Ma, F. Shi and Z. Q. Wang, *Chem. Mater.*, 2007, **19**, 1974–1978.
- 148 N. Sommerdijk and H. Colfen, *MRS Bull.*, 2011, **35**, 116–121.